ARL-TR-7895 ● Nov 2016

US Army Research Laboratory

Numeric Computation of the Radar Cross Section of In-flight Projectiles

by Traian Dogaru and Christopher Kenyon

Approved for public release; distribution unlimited.

NOTICES

Disclaimers

The findings in this report are not to be construed as an official Department of the Army position unless so designated by other authorized documents.

Citation of manufacturer's or trade names does not constitute an official endorsement or approval of the use thereof.

Destroy this report when it is no longer needed. Do not return it to the originator.

ARL-TR-7895 ● Nov 2016

US Army Research Laboratory

Numeric Computation of the Radar Cross Section of In-flight Projectiles

by Traian Dogaru and Christopher Kenyon
Sensors and Electron Devices Directorate, ARL

Approved for public release; distribution unlimited.

REPORT DOCUMENTATION PAGE

Form Approved
OMB No. 0704-0188

Public reporting burden for this collection of information is estimated to average 1 hour per response, including the time for reviewing instructions, searching existing data sources, gathering and maintaining the data needed, and completing and reviewing the collection information. Send comments regarding this burden estimate or any other aspect of this collection of information, including suggestions for reducing the burden, to Department of Defense, Washington Headquarters Services, Directorate for Information Operations and Reports (0704-0188), 1215 Jefferson Davis Highway, Suite 1204, Arlington, VA 22202-4302. Respondents should be aware that notwithstanding any other provision of law, no person shall be subject to any penalty for failing to comply with a collection of information if it does not display a currently valid OMB control number.
PLEASE DO NOT RETURN YOUR FORM TO THE ABOVE ADDRESS.

1. REPORT DATE *(DD-MM-YYYY)*	2. REPORT TYPE	3. DATES COVERED (From - To)
November 2016	Technical Report	Oct 2015–Sep 2016

4. TITLE AND SUBTITLE
Numeric Computation of the Radar Cross Section of In-flight Projectiles

5a. CONTRACT NUMBER

5b. GRANT NUMBER

5c. PROGRAM ELEMENT NUMBER

6. AUTHOR(S)
Traian Dogaru and Christopher Kenyon

5d. PROJECT NUMBER

5e. TASK NUMBER

5f. WORK UNIT NUMBER

7. PERFORMING ORGANIZATION NAME(S) AND ADDRESS(ES)
US Army Research Laboratory
ATTN: RDRL-SER-U
2800 Power Mill Road
Adelphi, MD 20783-1138

8. PERFORMING ORGANIZATION REPORT NUMBER
ARL-TR-7895

9. SPONSORING/MONITORING AGENCY NAME(S) AND ADDRESS(ES)

10. SPONSOR/MONITOR'S ACRONYM(S)

11. SPONSOR/MONITOR'S REPORT NUMBER(S)

12. DISTRIBUTION/AVAILABILITY STATEMENT
Approved for public release; distribution unlimited.

13. SUPPLEMENTARY NOTES

14. ABSTRACT
In this report, we evaluate the radar cross section (RCS) of in-flight ballistic projectiles (rockets, artillery rounds, and mortars) by taking into account the relative position and orientation of the targets with respect to a ground-based radar. The evaluation is based on computer models of both the ballistic trajectory and the radar scattering from the targets. Extensive theoretical derivations are developed, followed by numerical examples. We consider 2 types of projectiles: a 155-mm artillery round and a 120-mm mortar, as well as 4 radar frequency bands: L, S, C, and X. Using simulation tools entirely developed at the US Army Research Laboratory, we analyze several sample scenarios and discuss the phenomenological findings associated with them. The in-flight projectile RCS calculations will be used in future studies of radar system performance evaluation.

15. SUBJECT TERMS
computational electromagnetics, radar signature, ballistic trajectory, radar cross section, RCS

16. SECURITY CLASSIFICATION OF:			17. LIMITATION OF ABSTRACT	18. NUMBER OF PAGES	19a. NAME OF RESPONSIBLE PERSON
					Traian Dogaru
a. REPORT	b. ABSTRACT	c. THIS PAGE			19b. TELEPHONE NUMBER (Include area code)
Unclassified	Unclassified	Unclassified	UU	56	(301) 394-1482

Standard Form 298 (Rev. 8/98)
Prescribed by ANSI Std. Z39.18

Contents

List of Figures **iv**

List of Tables **v**

1. Introduction **1**

2. Calculation of In-Flight RCS of Projectiles **2**

2.1 General Methodology 2

2.2 Finding the Radar-Target Relative Orientation 5

2.3 Polarization Transformations 10

2.4 Propagation and Antenna Effects and the Radar Received Power 15

3. Simulation of Ballistics Trajectories **18**

3.1 The Modified Point Mass Model 18

3.2 Epicyclic Motion of Flying Projectiles 26

4. Numeric Examples **32**

4.1 Dynamic RCS of an In-Flight 155-mm Artillery Round 32

4.2 Dynamic RCS of an In-Flight 120-mm Mortar 39

5. Conclusions **43**

6. References **45**

List of Symbols, Abbreviations, and Acronyms **47**

Distribution List **48**

Approved for public release; distribution unlimited.

List of Figures

Fig. 1 The geometric configuration involved in the radar sensing of an in-flight ballistic projectile as seen in the ground reference frame x-y-z (or *G*).....2

Fig. 2 The radar targets in the i-j-k (or *P*) frame, showing the 155-mm artillery round (left) and the 120-mm mortar (right). When no spin, pitch, and yaw motions are accounted for, these pictures describe the radar-projectile relative orientation in the AFDTD radar signature models. The origin of the frame coincides with the projectile's center of mass. 3

Fig. 3 Flowchart describing the methodology of the dynamic RCS calculation for in-flight ballistic projectiles 5

Fig. 4 The in-flight 155-mm artillery round exhibiting the SPY motion components, shown here in the i-j-k (or *P*) frame (left) and the i_1-j_1-k_1 (or P_1) frame (right). In the left-hand picture, the k axis coincides with the projectile's velocity vector and the tangent to the trajectory. The picture on the right describes the final radar-projectile relative orientation in the AFDTD radar signature models. 9

Fig. 5 Diagrams showing the angles and unit vectors relevant to the polarization transformation calculation: a) view in the ground (*G*) frame and b) view in the projectile (P_1) frame 12

Fig. 6 The geometrical configuration involved in the calculation of the ballistic trajectory. The projectile axis coincides with the k_1 unit vector, while the velocity vector V has the same direction as the k unit vector. In this figure, the angle θ_B is negative. 20

Fig. 7 Various ways of describing the simulated 155-mm artillery round ballistic trajectory and its parameter variation vs. time: a) 3-D trajectory curve, b) height vs. range curve, c) velocity components vs. time, and d) projectile orientation angle ϕ_B vs. time. Figure 7a shows the approximate radar location in the simulations in Section 4.1. 25

Fig. 8 Various ways of describing the simulated 120-mm mortar ballistic trajectory and its parameter variation vs. time: a) 3-D trajectory curve, b) height vs. range curve, c) velocity components vs. time, and d) projectile orientation angle ϕ_B vs. time. Figure 8a shows the approximate radar location for the simulations in Section 4.2. 26

Fig. 9 Trajectory described by the 155-mm projectile tip in the i-j plane over a 1-s interval. a) 3-D view and b) view in the i-j plane. The pitch and yaw angles in Fig. 9a are exaggerated (not to scale). In Fig. 9b, the observer looks along the k axis, in the positive direction. 31

Fig. 10 Relative angles between the radar, projectile orientation, and ground obtained in the trajectory simulations of the 155-mm artillery round, showing: a) the ϕ_B, θ and γ angles, and b) the polarization rotation angle η 33

Approved for public release; distribution unlimited.

Fig. 11 Dynamic RCS vs. time curves obtained for the simulated trajectory of the 155-mm artillery round that does not account for the SPY motion components: a) L-band, b) S-band, c) C-band, and d) X-band.....34

Fig. 12 Dynamic RCS vs. time curves obtained for the simulated trajectory of the 155-mm artillery round that includes the SPY motion components: a) L-band, b) S-band, c) C-band, and d) X-band 35

Fig. 13 Received radar power vs. time for the in-flight 155-mm artillery round, assuming the fixed gain model in all 4 frequency bands, showing a) V-V polarization and b) H-H polarization 37

Fig. 14 Received radar power vs. time for the in-flight 155-mm artillery round, assuming the fixed aperture model in all 4 frequency bands, showing a) V-V polarization and b) H-H polarization.....37

Fig. 15 Propagation factor F^4 during the first 3 s of the 155-mm round ballistic flight, for all 4 frequency bands and a) V-V polarization and b) H-H polarization 38

Fig. 16 Received radar power during the first 3 s of the 155-mm artillery round ballistic flight, assuming the fixed gain model in all 4 frequency bands, showing a) V-V polarization and b) H-H polarization.....38

Fig. 17 Relative angles between the radar, projectile orientation, and ground obtained in the trajectory simulations of the 155-mm artillery round, showing a) the ϕ_B, θ, and γ angles and b) the ϕ angle for 2 values of χ_0.....40

Fig. 18 Dynamic RCS vs. time curves obtained for the simulated trajectory of the 120-mm mortar, comparing various ways to account for the initial roll angle χ_0, for V-V polarization and a) L-band, b) S-band, c) C-band, and d) X-band. Note: The curves obtained for L- and S-bands are on top of one another. 41

Fig. 19 Dynamic RCS vs. time curves obtained for the simulated trajectory of the 120-mm mortar, using the average over all possible angles χ_0, for a) L-band, b) S-band, c) C-band, and d) X-band 42

Fig. 20 Received radar power vs. time for the in-flight 120-mm mortar, assuming the fixed gain model in all 4 frequency bands, showing a) V-V polarization and b) H-H polarization 43

Fig. 21 Received radar power during the first 3 s of the 120-mm mortar ballistic flight, assuming the fixed gain model in all 4 frequency bands, showing a) V-V polarization and b) H-H polarization 43

List of Tables

Table 1 Physical parameters and initial conditions for the trajectory simulation examples in this section, involving a 155-mm artillery round and a 120-mm mortar 25

Approved for public release; distribution unlimited.

INTENTIONALLY LEFT BLANK.

Approved for public release; distribution unlimited.

1. Introduction

The US Army is actively pursuing the development of radar technology for the detection and tracking of artillery rounds grouped under the generic category of rockets, artillery, and mortar (RAM). The electromagnetic (EM) modeling team at the US Army Research Laboratory (ARL) is supporting these programs by modeling the radar signature of targets relevant to this application, which is a critical part of any radar system performance prediction study. This report continues previous work done at ARL related to RAM radar targets by considering their dynamic signature during the ballistic flight.

Very little work has been published on this topic in the past, particularly in the public domain. Otero et al.[1] provide a useful analysis of the RAM target radar cross section (RCS), including its variations for in-flight projectiles. However, no details are offered in that report related to the EM modeling codes used for radar signature prediction or the general methodology employed in computing the dynamic RCS of flying projectiles.

Our own previous investigations[2,3] analyzed the radar signature of RAM targets placed in a fixed position, using the AFDTD software developed at ARL.[4] To predict the signature of these targets during their ballistic flight, we need to develop models of their trajectories, as well as the geometric transformations that link the coordinate frames of the ground-based radar and the AFDTD signature simulations. While both these problems have been extensively investigated by other research communities (particularly those involved with ballistics and computer graphics, respectively), we are not aware of other documented work that brings these 2 engineering fields together with the radar signature analysis into one comprehensive study. Note that all the computer simulation codes employed in this work were developed entirely at ARL.

This report is organized as follows. In Section 2, we discuss the general methodology of in-flight projectile radar signature calculation, with emphasis on the geometrical transformations between the radar reference frame and the projectile coordinate frame. Section 3 discusses modeling ballistic trajectories, presenting the phenomenological aspects relevant to radar sensing of in-flight ballistic projectiles. In Section 4, we perform the numerical analysis of the dynamic radar signature for 2 types of projectiles: a 155-mm artillery round and a 120-mm mortar. We finish with conclusions in Section 5.

Approved for public release; distribution unlimited.

2. Calculation of In-Flight RCS of Projectiles

2.1 General Methodology

The radar sensing scenario under consideration in this report is described in Fig. 1. The radar system is placed in a stationary configuration at coordinates (x_R, y_R, z_R), whereas the projectile describes a time-dependent trajectory with instantaneous coordinates (x_P, y_P, z_P) of its center of mass. Additionally, the orientation of the projectile axis as a function of time must be specified. Our purpose is to compute the RCS of the in-flight projectile at a given sequence of time samples, as measured by the ground-based, stationary radar system.

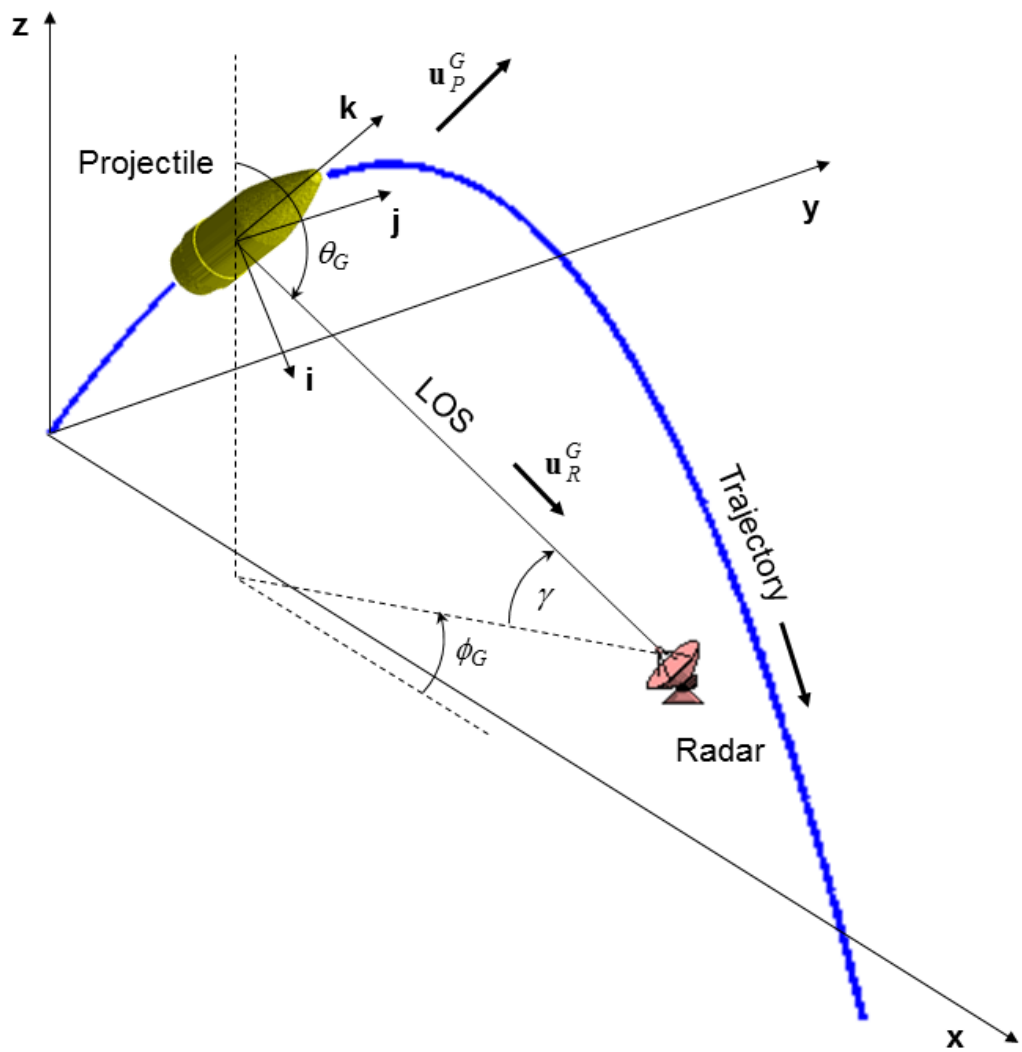

Fig. 1 The geometric configuration involved in the radar sensing of an in-flight ballistic projectile as seen in the ground reference frame x-y-z (or *G*)

The RCS calculation method starts with a characterization of the projectile's trajectory. This can be done either via computer simulations or measurements; in this study, we use models to compute the target's coordinates and orientation over the flight interval (see Section 3). Combining this information with the radar position, one can compute the relative radar-projectile orientation angles (more exactly, the angles between the radar line of sight [LOS] and the projectile symmetry axis) at each time sample. The geometrical transformations involved in this procedure are described in Section 2.2.

In previous work, we evaluated the radar signature of RAM projectiles in fixed positions, assuming the radar is placed at various angular coordinates on a sphere surrounding the target (Fig. 2). At each time sample of the projectile's flight, for the current radar-projectile aspect angle, the fixed-orientation signature data are used as a lookup table to compute the instantaneous RCS. Note that this procedure is independent of the radar signature evaluation method for the fixed position projectile: this can be obtained through measurements, numerical computations, or analytical approximations. In this study, we use data obtained via numerical simulation with the AFDTD software,[4] as described in our previous work.[2,3]

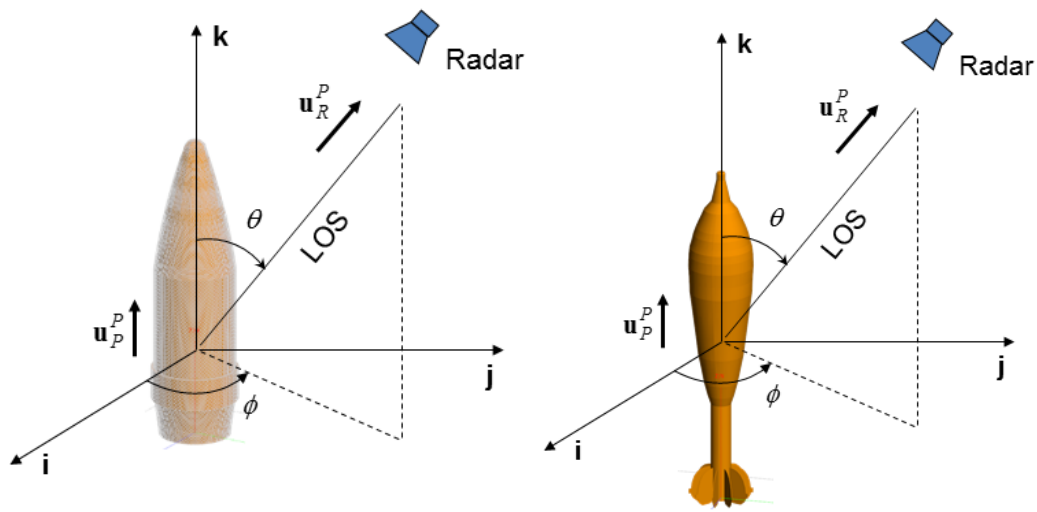

Fig. 2 The radar targets in the i-j-k (or *P*) frame, showing the 155-mm artillery round (left) and the 120-mm mortar (right). When no spin, pitch, and yaw motions are accounted for, these pictures describe the radar-projectile relative orientation in the AFDTD radar signature models. The origin of the frame coincides with the projectile's center of mass.

When transitioning from the fixed-orientation projectile to the in-flight projectile radar sensing scenarios, an additional complication arises due to the change in polarization of the radar waves between the 2 geometries. Typically, the radar signature is evaluated for a set of orthogonal polarization combinations (at the transmitter and receiver, respectively). In this case, we are interested in the vertical-

Approved for public release; distribution unlimited.

vertical (V-V) and horizontal-horizontal (H-H) polarizations. These polarizations are defined by the orientation of the electric-field vector in the radar (plane) wave with respect to the ground (or horizontal, or **x**-**y**) plane. Thus, the wave is horizontally polarized when the electric field is parallel to the ground plane and vertically polarized when the electric field is contained in the plane defined by the vertical axis (**z**) and the direction of propagation.[5]

A quick examination of the geometries in Figs. 1 and 2 reveals that the vertical and horizontal polarizations have completely different meanings in the 2 sensing scenarios. Consequently, when computing the radar signature of the in-flight target, the transformation from one coordinate system to the other must take into account not only the relative radar-target orientation, but the change in polarization as well. As shown in Section 2.3, the polarization transformations involve the full scattering matrix of the target,[6] which comprises the complex scattering parameters for each polarization combination, including vertical-horizontal (V-H) and horizontal-vertical (H-V).

So far, our discussion has been limited to the evaluation of the target response for this sensing scenario. Nevertheless, predicting the radar performance must take into account many other system parameters and environmental factors via the radar equation.[7,8] A full system performance analysis is beyond the scope of this report; however, we discuss some phenomenological aspects related to radar wave propagation and demonstrate how to calculate the radar received power for a given set of system parameters in Section 2.4. The signature analysis methodology described in this section is illustrated graphically in Fig. 3.

Approved for public release; distribution unlimited.

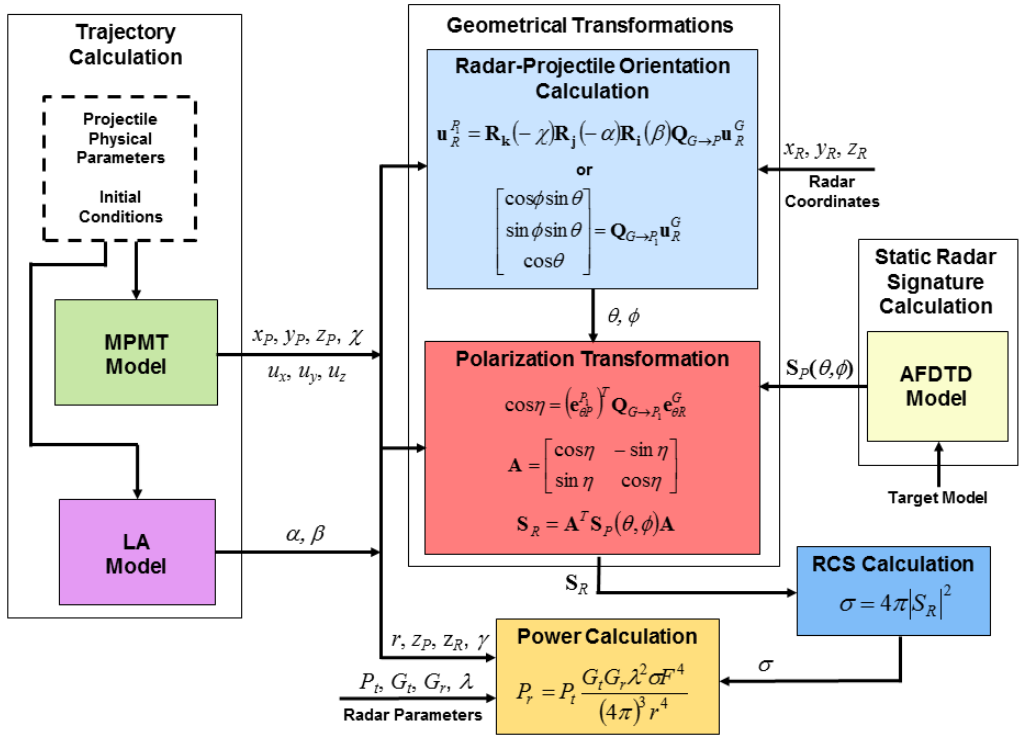

Fig. 3 Flowchart describing the methodology of the dynamic RCS calculation for in-flight ballistic projectiles

2.2 Finding the Radar-Target Relative Orientation

In this section, we derive the equations describing the relative orientation between the radar and the target, given the absolute coordinates of the 2, as well as the orientation of the target axis with respect to the ground. This problem can be solved by employing geometrical methods frequently used in computer graphics,[9] involving vector rotations in the 3-D space.

First, we need to introduce the notations describing the geometric transformations used in this section. These operations are usually performed on unit vectors in the 3-D space, defined by their components in a given Cartesian frame, for instance, the unit vector $\mathbf{u} = [a \quad b \quad c]^T$, with the constraint $a^2 + b^2 + c^2 = 1$. A rotation of angle α around an axis defined by its unit vector $\mathbf{w}$ is described by a 3 × 3 orthogonal matrix denoted by $\mathbf{R}_\mathbf{w}(\alpha)$. (Note: the angle α is considered positive when the rotation is performed counterclockwise as one looks against the direction of the $\mathbf{w}$ axis.) Thus, when we apply this transformation to an arbitrarily oriented unit vector $\mathbf{u}$, the result is the unit vector $\mathbf{v}$ given by $\mathbf{v} = \mathbf{R}_\mathbf{w}(\alpha)\mathbf{u}$. The rotation matrices have the following properties:

$$\mathbf{R}_{\mathbf{w}}(-\alpha)=\mathbf{R}_{\mathbf{w}}^{-1}(\alpha)=\mathbf{R}_{\mathbf{w}}^{T}(\alpha). \tag{1}$$

One can establish a general expression of the rotation matrix for an arbitrary direction of the rotation axis in space. However, in this report, we always attempt to reduce the problem to a sequence of rotations around one of the Cartesian axes (**x**, **y** or **z**). These rotations (of angle α) have the following simple expressions:

$$\mathbf{R}_{\mathbf{x}}(\alpha)=\begin{bmatrix}1 & 0 & 0\\ 0 & \cos\alpha & -\sin\alpha\\ 0 & \sin\alpha & \cos\alpha\end{bmatrix}, \tag{2}$$

$$\mathbf{R}_{\mathbf{y}}(\alpha)=\begin{bmatrix}\cos\alpha & 0 & \sin\alpha\\ 0 & 1 & 0\\ -\sin\alpha & 0 & \cos\alpha\end{bmatrix}, \tag{3}$$

$$\mathbf{R}_{\mathbf{z}}(\alpha)=\begin{bmatrix}\cos\alpha & -\sin\alpha & 0\\ \sin\alpha & \cos\alpha & 0\\ 0 & 0 & 1\end{bmatrix}. \tag{4}$$

Another frequently used concept is that of transformation from one Cartesian frame A to another frame B. This is described by an orthogonal matrix with the same properties as a rotation matrix and denoted $\mathbf{Q}_{A\to B}$. Thus, if the same unit vector in space $\mathbf{u}$ is written as $\mathbf{u}^A$ in frame A and as $\mathbf{u}^B$ in frame B, then we have $\mathbf{u}^B=\mathbf{Q}_{A\to B}\mathbf{u}^A$. The following important result is used in this study: The Cartesian frame transformation that takes the arbitrary unit vector $\mathbf{u}^A=\begin{bmatrix}a & b & c\end{bmatrix}^T$ (as expressed in frame A) to the **z** axis direction, $\mathbf{u}^B=\begin{bmatrix}0 & 0 & 1\end{bmatrix}^T$ (as expressed in frame B) is

$$\mathbf{Q}_{A\to B}=\begin{bmatrix}\dfrac{ac}{\sqrt{a^2+b^2}} & \dfrac{bc}{\sqrt{a^2+b^2}} & -\sqrt{a^2+b^2}\\ -\dfrac{b}{\sqrt{a^2+b^2}} & \dfrac{a}{\sqrt{a^2+b^2}} & 0\\ a & b & c\end{bmatrix}. \tag{5}$$

Now let us apply this formula to the 2 Cartesian frames described in Figs. 1 and 2. We call the frame in Fig. 1 the "ground" frame, denoted by superscript G, and the frame in Fig. 2 the "projectile" frame, denoted by superscript P. Notice that the

Approved for public release; distribution unlimited.

projectile axis direction coincides with the **k** axis in frame *P*, meaning that its unit vector is $\mathbf{u}_P^P = \begin{bmatrix} 0 & 0 & 1 \end{bmatrix}^T$. Therefore, if the same projectile axis is expressed as $\mathbf{u}_P^G = \begin{bmatrix} u_x & u_y & u_z \end{bmatrix}^T$ in frame *G*, the matrix describing the transformation between the 2 frames is

$$\mathbf{Q}_{G\to P} = \begin{bmatrix} \dfrac{u_x u_z}{\sqrt{u_x^2 + u_y^2}} & \dfrac{u_y u_z}{\sqrt{u_x^2 + u_y^2}} & -\sqrt{u_x^2 + u_y^2} \\ -\dfrac{u_y}{\sqrt{u_x^2 + u_y^2}} & \dfrac{u_x}{\sqrt{u_x^2 + u_y^2}} & 0 \\ u_x & u_y & u_z \end{bmatrix} . \tag{6}$$

Let $\mathbf{u}_R$ the unit vector describing the direction of the radar LOS to the projectile position. Given the sets of coordinates (x_R, y_R, z_R) and (x_P, y_P, z_P) in Fig. 1, as well as the angles θ and ϕ in Fig. 2, we can express this unit vector in the 2 frames as follows:

$$\mathbf{u}_R^G = \frac{1}{\sqrt{(x_R - x_P)^2 + (y_R - y_P)^2 + (z_R - z_P)^2}} \begin{bmatrix} x_R - x_P \\ y_R - y_P \\ z_R - z_P \end{bmatrix} , \tag{7}$$

$$\mathbf{u}_R^P = \begin{bmatrix} \cos\phi \sin\theta \\ \sin\phi \sin\theta \\ \cos\theta \end{bmatrix} . \tag{8}$$

We use the matrix in Eq. 6 to derive the transformation from $\mathbf{u}_R^G$ to $\mathbf{u}_R^P$, as one transitions from frame *G* to frame *P*:

$$\mathbf{u}_R^P = \begin{bmatrix} a \\ b \\ c \end{bmatrix} = \mathbf{Q}_{G\to P} \mathbf{u}_R^G . \tag{9}$$

Once we determine the components *a*, *b*, and *c* of $\mathbf{u}_R^P$, the angles θ and ϕ are found as

$$\theta = \cos^{-1} c , \tag{10}$$

Approved for public release; distribution unlimited.

$$\phi = \tan^{-1} \frac{b}{a} \ . \tag{11}$$

These 2 angles are used as indexes in the RCS lookup table obtained from the AFDTD simulations, as discussed in the previous section. Interpolation can be used when the values computed in Eqs. 10 and 11 fall in between the angle increments used in the AFDTD simulations. So far, the evaluation of the radar LOS angles required knowledge of the radar coordinates (x_R, y_R, z_R) (fixed in time), as well as the projectile coordinates (x_P, y_P, z_P) and orientation (u_x, u_y, u_z) with respect to the ground frame, which are variable in time and are specified in a separate file describing the projectile trajectory.

As illustrated in Section 3, the ballistic trajectories obtained by computer simulations are frequently based on the modified point mass model,[10] in which the projectile orientation unit vector closely follows the tangent to the trajectory (or the velocity vector direction). In this simplified model, the projectile symmetry axis coincides with the velocity vector direction (same as the **k** axis of the *P* frame in Fig. 2), so (u_x, u_y, u_z) represent the velocity vector components normalized to this vector's magnitude. In reality, the projectile motion is more complex and its complete characterization requires a 6 degrees-of-freedom (DOF) model framework.[10] Since we do not have access to the 6 DOF trajectory data, our simulation strategy involves separately adding spin, pitch, and yaw (SPY) motion components to the trajectory data obtained via the modified point mass model (see Section 3 for more details). In the following, we call *P* the frame where the projectile velocity vector (or tangent to the trajectory) is aligned with the vertical axis, and P_1 the frame where the projectile axis after SPY is aligned with the vertical axis. The difference between these 2 frames is illustrated in Fig. 4.

Approved for public release; distribution unlimited.

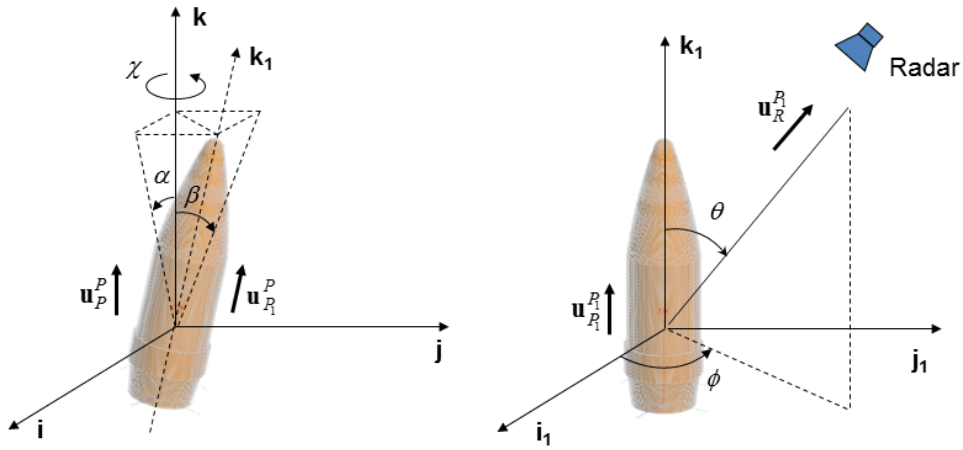

Fig. 4 The in-flight 155-mm artillery round exhibiting the SPY motion components, shown here in the i-j-k (or *P*) frame (left) and the i_1-j_1-k_1 (or P_1) frame (right). In the left-hand picture, the k axis coincides with the projectile's velocity vector and the tangent to the trajectory. The picture on the right describes the final radar-projectile relative orientation in the AFDTD radar signature models.

The spinning motion component can be described as a rotation of the projectile in vertical orientation (as in Fig. 2), around the **k** axis and of angle χ. The pitch and yaw motion components can be described by a sequence of 2 rotations of the projectile axis: one around the **j** axis (of angle α), followed by one around the **i** axis (of angle $-\beta$). As a side note, switching the order of the last 2 rotations leads to slightly different results, since rotations are noncommutative; however, given the fact that α and β are small, both rotation sequences can be approximated by the same matrix, so the order does not matter. The time dependence of these 3 motion components is discussed in Section 3. Call the unit vector of the new projectile orientation (after the 3 SPY rotations) $\mathbf{u}_{P_1}$, coinciding the $\mathbf{k}_1$ axis direction. In frame *P*, this is given by

$$\mathbf{u}_{P_1}^{P} = \mathbf{R}_{\mathbf{i}}(-\beta)\mathbf{R}_{\mathbf{j}}(\alpha)\mathbf{R}_{\mathbf{k}}(\chi)\mathbf{u}_{P}^{P} \ . \tag{12}$$

Expressing the unit vector of the projectile axis prior to the 3 additional rotations $\mathbf{u}_P$, in the new P_1 frame, involves performing the inverse of the 3 rotations in reverse order:

$$\mathbf{u}_{P}^{P_1} = \mathbf{R}_{\mathbf{k}}(-\chi)\mathbf{R}_{\mathbf{j}}(-\alpha)\mathbf{R}_{\mathbf{i}}(\beta)\mathbf{u}_{P}^{P} \ . \tag{13}$$

Combining this with previous results, the transformation matrix from the *G* frame to the P_1 frame becomes

$$\mathbf{Q}_{G\to P_1} = \mathbf{R}_{\mathbf{k}}(-\chi)\mathbf{R}_{\mathbf{j}}(-\alpha)\mathbf{R}_{\mathbf{i}}(\beta)\mathbf{Q}_{G\to P} \tag{14}$$

Approved for public release; distribution unlimited.

and, finally,

$$\mathbf{u}_R^{P_1} = \mathbf{R}_\mathbf{k}(-\chi)\mathbf{R}_\mathbf{j}(-\alpha)\mathbf{R}_\mathbf{i}(\beta)\mathbf{Q}_{G\to P}\mathbf{u}_R^G \ . \tag{15}$$

The calculation of the unit vector $\mathbf{u}_R^{P_1}$ components allows the evaluation of the radar LOS angles θ and ϕ with respect to the instantaneous projectile axis, after accounting for the 3 additional SPY motion components, by using Eqs. 10 and 11.

2.3 Polarization Transformations

Since the EM field is a vector quantity, the full characterization of the target response involves the links between all components of the incident and scattered electric-field vectors. This is usually expressed by the 2 × 2 scattering matrix of the target,[6] **S**, defined by

$$\mathbf{E}^s = \frac{e^{-jk_0 r}}{r}\mathbf{S}\mathbf{E}^i \tag{16}$$

or

$$\begin{bmatrix} E_\theta^s \\ E_\phi^s \end{bmatrix} = \frac{e^{-jk_0 r}}{r}\begin{bmatrix} S_{\theta\theta} & S_{\theta\phi} \\ S_{\phi\theta} & S_{\phi\phi} \end{bmatrix}\begin{bmatrix} E_\theta^i \\ E_\phi^i \end{bmatrix} \ . \tag{17}$$

In these equations, the superscript s indicates scattered field, while the superscript i indicates incident field; r is the radar-target range and k_0 is the propagation constant. Notice that we use the θ and ϕ components of the electric field instead of the traditional vertical and horizontal components, since the latter are typically defined with respect to a fixed ground plane. In our analysis, where we use different reference frames, with different orientations with respect to the ground, these traditional definitions are less meaningful.

Our task in this section is to find the transformation of the scattering matrix from a hypothetical radar placed in the projectile frame (call this $\mathbf{S}_P$) to the ground-based actual radar frame (call this $\mathbf{S}_R$). The former is computed in the AFDTD simulations of the target signature, whereas the latter describes the in-flight target response as measured by the ground-based radar. All the relevant geometries are illustrated in Fig. 5. Notice that in both frames (P_1 and G), the far-field electric-field vector of the radar waves (both incident and scattered) is perpendicular to the LOS, so only 2 of its components (θ and ϕ) need to be considered, as in Eq. 17. The far-field scattering model in this study assumes plane wave propagation and linear polarization, meaning that the electric-field vectors (incident and scattered) keep

the same orientation and magnitude along the propagation path. We decompose the electric-field vectors in the 2 frames along the 2 components, θ and ϕ. As shown in Fig. 5a, these components have different directions between the 2 frames. The relationships between the electric-field vectors in the 2 radar frames can be written as

$$\mathbf{E}_P^i = \begin{bmatrix} E_{\theta P}^i \\ E_{\phi P}^i \end{bmatrix} = \mathbf{A}\mathbf{E}_R^i = \mathbf{A}\begin{bmatrix} E_{\theta R}^i \\ E_{\phi R}^i \end{bmatrix}, \tag{18}$$

$$\mathbf{E}_P^s = \begin{bmatrix} E_{\theta P}^s \\ E_{\phi P}^s \end{bmatrix} = \mathbf{A}\mathbf{E}_R^s = \mathbf{A}\begin{bmatrix} E_{\theta R}^s \\ E_{\phi R}^s \end{bmatrix}, \tag{19}$$

where $\mathbf{A}$ is a 2 × 2 orthogonal matrix, with the following elements:

$$\mathbf{A} = \begin{bmatrix} \cos\eta & \sin\eta \\ -\sin\eta & \cos\eta \end{bmatrix}. \tag{20}$$

Notice that $\mathbf{E}_P^{i(s)}$ and $\mathbf{E}_R^{i(s)}$ represent the same vectors in space, although their θ and ϕ components change with the reference frame according to Eqs. 18 and 19.

Approved for public release; distribution unlimited.

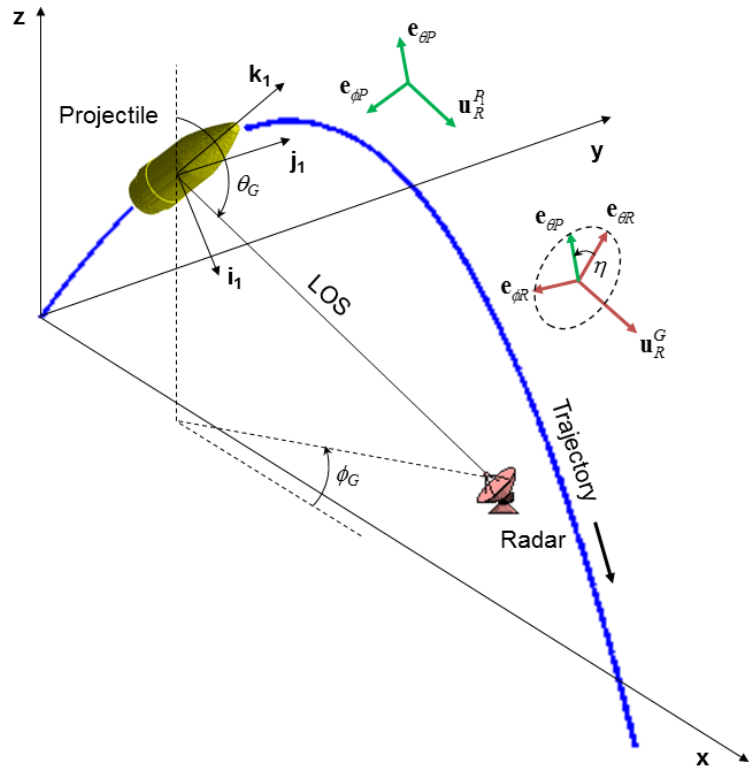

(a)

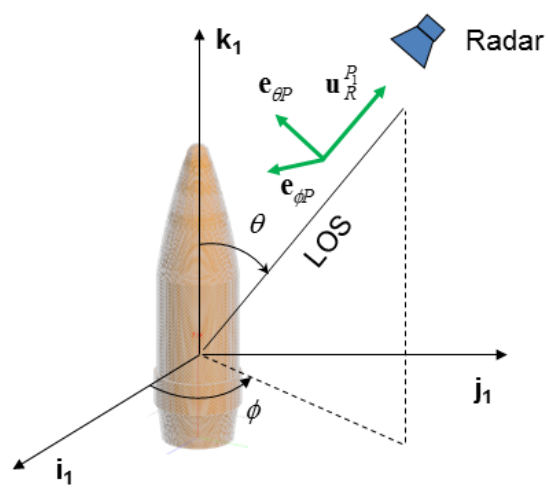

(b)

Fig. 5 Diagrams showing the angles and unit vectors relevant to the polarization transformation calculation: a) view in the ground (*G*) frame and b) view in the projectile (*P*1) frame

The angle η can be derived from

$$\cos\eta = \left(\mathbf{e}_{\theta P}\right)^T \mathbf{e}_{\theta R} \ . \tag{21}$$

In the last equation, $\mathbf{e}_{\theta P}$ and $\mathbf{e}_{\theta R}$ are the unit vectors of the θ electric-field components in the P_1 and G frames, respectively (notice that we dropped the i or s superscript, since the quantities are identical for the incident and scattered fields; this is consistent with the monostatic radar assumption and the sign conventions used by the AFDTD software). The scattering matrix transformation can be derived by writing

$$\mathbf{E}_R^s = \mathbf{A}^T \mathbf{E}_P^s = \mathbf{A}^T \frac{e^{-jk_0 r}}{r} \mathbf{S}_P \mathbf{E}_P^i = \frac{e^{-jk_0 r}}{r} \mathbf{A}^T \mathbf{S}_P \mathbf{A} \mathbf{E}_R^i = \frac{e^{-jk_0 r}}{r} \mathbf{S}_R \mathbf{E}_R^i \quad , \tag{22}$$

which leads to

$$\mathbf{S}_R = \mathbf{A}^T \mathbf{S}_P \mathbf{A} \ . \tag{23}$$

To perform the scattering matrix transformation in Eq. 23, all we need is the $\cos\eta$ parameter, defined in Eq. 21. So far, we have not used the superscripts G or P_1 to denote a specific set of coordinates for any of the vectors introduced in this section. In the following, we specifically use these superscripts G and P_1 for the $\mathbf{e}_{\theta P}$ and $\mathbf{e}_{\theta R}$ unit vectors (remember that in the P_1 frame the projectile axis is aligned with the vertical axis, after taking into account the SPY motion components). When we take the scalar product of $\mathbf{e}_{\theta P}$ and $\mathbf{e}_{\theta R}$ in Eq. 21, we must make sure that both unit vectors are expressed relative to the same frame.

When the direction of propagation (or radar-target LOS) in the ground frame is defined by the elevation angle θ_G and azimuth angle ϕ_G, the θ component of the electric field (as expressed in the ground frame) has the unit vector[5]

$$\mathbf{e}_{\theta R}^G = \begin{bmatrix} -\cos\theta_G \cos\phi_G \\ -\cos\theta_G \sin\phi_G \\ \sin\theta_G \end{bmatrix} , \tag{24}$$

where

$$\cos\theta_G = \frac{z_R - z_P}{\sqrt{(x_R - x_P)^2 + (y_R - y_P)^2 + (z_R - z_P)^2}} \ , \tag{25}$$

$$\sin\theta_G = \frac{\sqrt{(x_R - x_P)^2 + (y_R - y_P)^2}}{\sqrt{(x_R - x_P)^2 + (y_R - y_P)^2 + (z_R - z_P)^2}} \ , \tag{26}$$

$$\cos\phi_G = \frac{x_R - x_P}{\sqrt{(x_R - x_P)^2 + (y_R - y_P)^2}} \ , \tag{27}$$

$$\sin\phi_G = \frac{y_R - y_P}{\sqrt{(x_R - x_P)^2 + (y_R - y_P)^2}} \ . \tag{28}$$

The signs in Eq. 24 were chosen consistent with the conventions used by the AFDTD software. Transforming this unit vector to the projectile frame is done via

$$\mathbf{e}_{\theta R}^{P_1} = \mathbf{Q}_{G\to P_1}\mathbf{e}_{\theta R}^{G} \ , \tag{29}$$

with $\mathbf{Q}_{G\to P_1}$ given by Eq. 14. By a similar argument, the unit vector $\mathbf{e}_{\theta P}^{P_1}$ in the P_1 frame (Fig. 5b) is given by

$$\mathbf{e}_{\theta P}^{P_1} = \begin{bmatrix} -\cos\theta\cos\phi \\ -\cos\theta\sin\phi \\ \sin\theta \end{bmatrix} , \tag{30}$$

where the angles θ and ϕ are given by Eqs. 10 and 11. It follows that

$$\cos\eta = \left(\mathbf{e}_{\theta P}^{P_1}\right)^T \mathbf{e}_{\theta R}^{P_1} = \left(\mathbf{e}_{\theta P}^{P_1}\right)^T \mathbf{Q}_{G\to P_1}\mathbf{e}_{\theta R}^{G} \ . \tag{31}$$

The last equation allows the computation of $\mathbf{A}$ and $\mathbf{S}_R$ via Eqs. 20 and 23, respectively.

The entire in-flight target signature calculation procedure presented in the last 2 sections can be summarized as follows:

- For each time sample, read the projectile coordinates (x_P, y_P, z_P) and velocity orientation (u_x, u_y, u_z) from the trajectory file. Additionally, compute the angles χ, α and β describing the SPY motions.
- Compute the angles θ and ϕ by Eqs. 15, 10, and 11.
- In the AFDTD target response simulation data, select the scattering matrix $\mathbf{S}_P$ corresponding to the angles θ and ϕ.
- Use Eqs. 24–28, 30–31, 20, and 23 (in this order) to compute the scattering matrix $\mathbf{S}_R$ characterizing the target response in the ground-based radar frame.

- Compute the instantaneous target RCS for each polarization combination as $\text{RCS} = 4\pi|S_R|^2$, where S_R is the corresponding scattering matrix element.

2.4 Propagation and Antenna Effects and the Radar Received Power

The procedure outlined in the previous 2 sections allows the complete characterization of the in-flight target signature as measured by the ground-based radar system. However, to predict the radar system performance, many other parameters (related to system design, propagation environment, and signal processing) must be taken into account. This is done via the radar equation.[7,8]

There are many possible forms of the radar equation, involving various levels of detail of the system design, and tailored to various radar operational modes or applications. In this section, we use a relatively simple form of the equation that allows the calculation of the radar received power, based on the target trajectory and its radar signature, computed by the procedure described in Section 2.3.

For a ground-based radar system designed to search and track RAM projectiles at medium to large ranges, the elevation angles (as measured from the ground plane) can be very small, on the order of a few degrees or less. In this case, the ground bounce of the radar waves can have a strong effect on the radar received power. This is usually accounted for by the propagation factor F^4 in the radar equation.[7] If one includes this factor, the radar received power is computed as

$$P_r = P_t \frac{G_t G_r \lambda^2 \sigma F^4}{(4\pi)^3 r^4} \quad . \tag{32}$$

In this equation, P_t and P_r are the transmitted and received powers, respectively; G_t and G_r are the transmitter and receiver antenna gains, respectively; λ is the wavelength; σ is the RCS; and $r = \sqrt{(x_R - x_P)^2 + (y_R - y_P)^2 + (z_R - z_P)^2}$ is the radar-target range. The usual assumption is that the radar tracks the target within its main antenna beam and the gain is computed at boresight. Another possible form that uses the antenna effective aperture A instead of the gain is

$$P_r = P_t \frac{A_t A_r \sigma F^4}{4\pi\lambda^2 r^4} \quad . \tag{33}$$

For a grazing angle γ, the F factor is given by[8]

$$F = \left| 1 + \frac{G(2\gamma)}{G(0)} \Gamma(\gamma) \exp\left(-j \frac{4\pi z_P z_R}{\lambda r} \right) \right| , \tag{34}$$

where the antenna gain G is computed at boresight and at an angle 2γ away from boresight, and $\Gamma(\gamma)$ is the Fresnel reflection coefficient of the ground for a grazing angle γ. All the other parameters in Eq. 34 were defined previously. For reference, the reflection coefficient is given by[7]

$$\Gamma_V(\gamma) = \frac{\varepsilon_r \sin\gamma - \sqrt{\varepsilon_r - \cos^2\gamma}}{\varepsilon_r \sin\gamma + \sqrt{\varepsilon_r - \cos^2\gamma}} , \tag{35}$$

for vertical polarization, and

$$\Gamma_H(\gamma) = \frac{\sin\gamma - \sqrt{\varepsilon_r - \cos^2\gamma}}{\sin\gamma + \sqrt{\varepsilon_r - \cos^2\gamma}} , \tag{36}$$

for horizontal polarization, where ε_r is the complex dielectric constant of the ground, and γ is given by

$$\gamma = \sin^{-1} \frac{z_P - z_R}{r} . \tag{37}$$

As shown in the numerical examples in Section 4, the propagation factor has an important impact (meaning it deviates significantly from 1) only for very small values of γ (typically, less than 1°). In practice, this impacts the radar received power only during the first few seconds of the projectile's trajectory. However, its effect on the detection performance may be important from a radar system operational standpoint, because during that time interval the radar works in search mode, when target detection represents its most critical function.

The propagation factor F^4 may depend on various EM phenomena other than the ground bounce of radar waves.[7] Thus, atmospheric effects tend to distort the propagation paths due to variations in the refraction index of the medium. The Earth's curvature can also affect the propagation factor, although its impact is significant only at very long ranges (on the order of 100 km or longer). Additionally, irregularities and objects on the ground surface (hills/valleys, buildings, vegetation, etc.) introduce both distortions in the radar wave propagation and direct scattering back to the radar, with a profound impact on the radar detection performance. Since all these effects are site-specific, they are not considered in this

Approved for public release; distribution unlimited.

investigation. However, any complete radar performance prediction model would have to take them into account.

Another EM analysis aspect that has an effect on the radar equation is the radar antenna polarization. This is characterized by the antenna effective length,[11] **h**, defined as

$$\mathbf{E}^i = \frac{jZ_0 I_{sc}}{2\lambda r} e^{-jk_0 r} \mathbf{h}_t \ , \tag{38}$$

for the transmitter antenna, and

$$V_o = \mathbf{h}_r^H \mathbf{E}^s \ , \tag{39}$$

for the receiver antenna. In the last 2 equations, Z_0 is the free-space impedance, I_{sc} is the short-circuit current of the transmitter antenna, and V_o is the open-circuit voltage of the receiver antenna. Also notice that we used the superscript H (from Hermitian) to denote the transpose-conjugate of the $\mathbf{h}_r$ vector in Eq. 39, since this vector may have complex components. The effective lengths $\mathbf{h}_t$ and $\mathbf{h}_r$ include information on both the antenna gains and polarization vectors, and are functions of the elevation and azimuth angles with respect to the antenna's boresight direction (θ_A and ϕ_A, respectively). After some manipulations, one can show[12] that, to account for both the antenna polarization and the target polarimetric scattering effects, the product $G_t G_r \sigma$ in the radar equation must be replaced by

$$\frac{4\pi}{\lambda^2} \left| \mathbf{h}_r^H \mathbf{S} \mathbf{h}_t \right|^2 . \tag{40}$$

This results is in contrast to the case of either vertically or horizontally polarized antennas, described in Section 2.3, where σ was simply replaced by $4\pi|S|^2$, with S being a scalar element of the scattering matrix.

This kind of analysis is particularly important in radar systems that use antenna arrays (of fixed orientation) and electronic scanning. Although the antenna elements are typically designed to transmit and receive either vertically or horizontally polarized waves at boresight, the wave polarization becomes mixed for a beam squinted away from boresight. In that case, one must use the expression in Eq. 40, with $\mathbf{h}_t$ and $\mathbf{h}_r$ functions of both θ_A and ϕ_A. Additional corrections related to the so-called *cosine* loss[7] are also needed for the antenna gain when the beam points away from boresight. All these effects are dependent on the radar antenna design (both at element and array levels) and are not pursued in the numeric

examples included in this study. Nevertheless, they are important factors the radar designer must take into account when evaluating overall system performance.

3. Simulation of Ballistics Trajectories

3.1 The Modified Point Mass Model

In this section, we discuss the ballistic trajectories of symmetric artillery and mortar rounds (notice that projectiles equipped with rocket engines are not treated in this report). The exterior ballistics of projectiles is a mature and complex engineering subject—its detailed presentation is clearly beyond the scope of this investigation. However, an introduction to the motion equations governing ballistic projectiles, as well as their solutions (analytic or numeric), reveals interesting phenomenological aspects that are relevant to the radar sensing of these targets. Our purpose here is to develop a numeric model of the ballistic projectile flying motion that can be used in predicting its radar signature. Two types of projectiles are considered in this study: spin-stabilized projectiles (such as Howitzer-launched artillery shells) and fin-stabilized projectiles (such as mortar rounds). The material in Section 3 is based on a selection of earlier studies[10,13–15]; interestingly, some of the most important developments in ballistic science since World War II were made at the Ballistic Research Laboratory (BRL), which later became part of the current ARL.

The most complete description of the ballistic projectile motion after it leaves the gun barrel and until it hits the target is given by the 6 DOF model.[10,13] This represents a system of 6 coupled first-order nonlinear differential equations: 3 for the time derivatives of the linear momentum (or velocity) components and 3 for the time derivatives of the angular momentum components. The equations can be formally written in vector forms as

$$m\frac{d\mathbf{V}}{dt} = \sum \mathbf{F} + m\mathbf{g} + m\mathbf{\Lambda}\,, \tag{41}$$

$$\frac{d\mathbf{H}}{dt} = \sum \mathbf{M}\,. \tag{42}$$

As a general note, in Section 3, we mostly use the symbols and notations in McCoy,[10] with the exception of the Cartesian frame axis names (both the ground and projectile frames). For the latter, we use notations consistent with Section 2 of this report. Other variable names in this section may coincide but should not be

confused with the notations in Section 2. On occasions, we use the dot symbol (e.g., $\dot{V} = \frac{dV}{dt}$) to denote the time derivative of a motion variable.

In Eqs. 41 and 42, **V** is the vector velocity of the center of mass with respect to the ground, m is the projectile mass, **g** is the gravitational acceleration, $\mathbf{\Lambda}$ is the Coriolis acceleration,[10] and **H** is the total vector angular momentum. The quantities on the right-hand sides of the 2 equations include the sum of all aerodynamic forces **F** and the sum of all aerodynamic moments **M** acting on the projectile. Since we do not intend to go into a detailed description of the 6 DOF model, we do not explicitly write the equations for all forces and moments, but simply enumerate them instead, as follows[10]:

- Forces: drag force, lift force, Magnus force, pitch damping force
- Moments: spin damping moment, rolling moment due to fin cant, pitching (overturning) moment, Magnus moment, pitch damping moment

If **W** is the vector wind velocity (relative to the ground frame), then the relative velocity of the projectile with respect to air is $\mathbf{v} = \mathbf{V} - \mathbf{W}$. In the rest of this study, we assume that there is no wind (**W** = 0), so **v** and **V** coincide. For nonzero wind speed conditions, the vector **V** should be replaced by **v** in the expressions of all aerodynamic forces and moments. Note that the direction of **V** is also the vector tangent to the trajectory.

A graphic representation of the various coordinate systems used in this section is shown in Fig. 6. The **x-y-z** frame (or *G* frame) is the usual Cartesian frame attached to the ground, while the frame **i-j-k** (or *P* frame) is attached to the velocity vector **V** as follows: **k** has the same direction as **V**, **j** is in the horizontal plane and perpendicular to **k**, while **i** is perpendicular on both **k** and **j** and contained in a vertical plane ($\mathbf{i} = \mathbf{j} \times \mathbf{k}$). Notice that the projectile axis (described by the unit vector $\mathbf{k}_1$) and the velocity vector **V** direction are not necessarily identical; the angle between the 2, α_t, is called the angle of attack. The elevation and azimuth angles made by the **V** vector with the **x-y-z** frame are ϕ_B and θ_B, as in Fig. 6 (note that these angles are defined differently from the elevation and azimuth angles in Section 2).

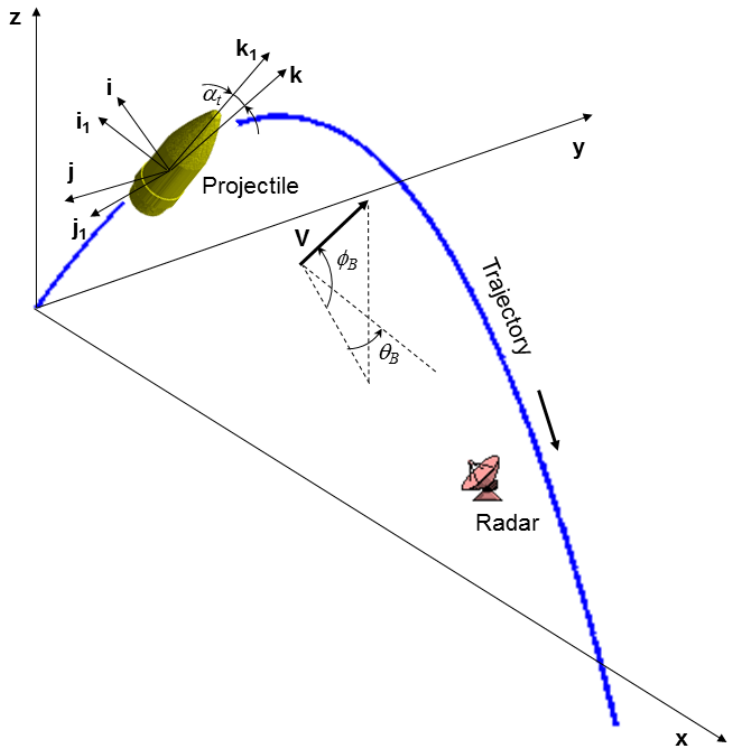

Fig. 6 The geometrical configuration involved in the calculation of the ballistic trajectory. The projectile axis coincides with the k_1 unit vector, while the velocity vector V has the same direction as the k unit vector. In this figure, the angle θ_B is negative.

The numerical integration of the differential equations Eqs. 41 and 42 involved in the 6 DOF model is discussed in McCoy.[10] Nevertheless, we chose not to pursue this model in our ballistic trajectory study for 2 reasons: 1) we did not have ready access to a 6 DOF simulation code and 2) as discussed elsewhere,[10,13] the full 6 DOF model is not really necessary to model the trajectory of symmetric projectiles, except in very particular cases, which are not relevant to most practical scenarios. Instead, we investigate the modified point-mass trajectory (MPMT) model,[10,13–15] combined with the epicyclic motion derived from the linearized aeroballistic (LA) model.[10,13] As pointed out in McCoy,[10] simulations by the MPMT model yield trajectories almost identical to the 6 DOF model in most scenarios of interest; however, the MPMT model does not completely characterize the pitching and yawing (or epicyclic) motions of the projectile. The epicyclic projectile motion, which has an important impact on the radar signature, is treated separately by an analytic approximation and combined with the other trajectory parameters derived from the MPMT model to create a more realistic representation of the projectile flight.

In the MPMT model, the linear momentum (or velocity) equations are preserved as in the 6 DOF model, but, from the 3 angular momentum equations, only the one

describing the roll (or spin) motion is preserved as fully coupled with the 3 velocity equations. The other 2 types of rotational motion, pitching and yawing, involve a transient and a steady-state component—these are described in more detail in Section 3.2. The main simplification in the MPMT model consists of neglecting the transient pitch-yaw motion (in the assumption that its amplitude is very small) and preserving only the steady-state component, described by the vector $\boldsymbol{\alpha}_R$, called the yaw of repose. This variable is inserted back in the remaining 4 differential equations; however, the calculation of $\boldsymbol{\alpha}_R$ as a function of the other motion parameters involves a simple algebraic expression, as compared to the additional differential equations required by the 6 DOF model.

Specifically, the equations describing the MPMT model can be written as follows[10]:

$$\frac{d\mathbf{V}}{dt} = -\frac{\rho S C_D}{2m} v\mathbf{v} + \frac{\rho S C_{L\alpha}}{2m} v^2 \boldsymbol{\alpha}_R + \frac{\rho S C_{Np\alpha}}{2m} p\left(\mathbf{v} \times \boldsymbol{\alpha}_R\right) + \mathbf{g} + \boldsymbol{\Lambda} \ , \quad (43)$$

$$\frac{dp}{dt} = \frac{\rho S d^2 v}{2I_R} p C_{lp} \ , \quad (44)$$

The approximate equation governing the yaw of repose takes different forms for spin- and fin-stabilized projectiles. Thus, in the case of spin stabilization,

$$\boldsymbol{\alpha}_R = \frac{2I_x p\left(\mathbf{g} \times \mathbf{v}\right)}{\rho S d v^4 C_{M\alpha}} \ , \quad (45a)$$

while for fin stabilization,

$$\boldsymbol{\alpha}_R = \frac{C_{Mq} d\left(\mathbf{v} \times \left(\mathbf{v} \times \mathbf{g}\right)\right)}{v^4 C_{M\alpha}} \ . \quad (45b)$$

In Eq. 43, the accelerations produced by the drag, lift, and Magnus forces were written explicitly as the first 3 terms in the right-hand side. In Eqs. 43–45, we introduced the following notations: p for the spin rate (or angular velocity), ρ for the air density, S for the projectile's cross-sectional area, I_R for its axial moment of inertia, d for its diameter (or caliber), C_D for the drag force coefficient, $C_{L\alpha}$ for the lift force coefficient, $C_{Np\alpha}$ for the Magnus force coefficient, C_{lp} for the spin damping moment coefficient, C_{Mq} for the pitch damping moment coefficient, and $C_{M\alpha}$ for the pitching (or overturning) moment coefficient. The following forces and moments are neglected in this model: the pitch damping force, the rolling moment due to fin cant (assuming there is no fin cant), and the Magnus moment. As

mentioned earlier, we assume there is no wind, so we can replace **v** by **V** in Eqs. 43–45.

By explicitly writing the equations for each velocity component, and neglecting the Coriolis acceleration, we obtain the following system of 4 scalar differential equations:

$$\dot{V}_x = -\frac{\rho S C_D}{2m} V V_x + \frac{\rho S C_{L\alpha}}{2m} V^2 \alpha_{Rx} + \frac{\rho S C_{Np\alpha}}{2m} p\left(V_y \alpha_{Rz} - V_z \alpha_{Ry}\right) , \quad (46a)$$

$$\dot{V}_y = -\frac{\rho S C_D}{2m} V V_y + \frac{\rho S C_{L\alpha}}{2m} V^2 \alpha_{Ry} + \frac{\rho S C_{Np\alpha}}{2m} p\left(V_z \alpha_{Rx} - V_x \alpha_{Rz}\right) , \quad (46b)$$

$$\dot{V}_z = -\frac{\rho S C_D}{2m} V V_z + \frac{\rho S C_{L\alpha}}{2m} V^2 \alpha_{Rz} + \frac{\rho S C_{Np\alpha}}{2m} p\left(V_x \alpha_{Ry} - V_y \alpha_{Rx}\right) - g , \quad (46c)$$

$$\dot{p} = \frac{\rho S d^2 V}{2 I_R} p C_{lp} , \quad (46d)$$

with $V = \sqrt{V_x^2 + V_y^2 + V_z^2}$.

One phenomenon with significant effect on ballistic trajectories is the variation of air pressure with altitude (height). A simple equation accurately describing this variation for altitudes z up to 6 km is[10]

$$\rho(z) = \rho_0 e^{-hz} , \quad (47)$$

where ρ_0 = 1.225 kg/m^3 is the air pressure at sea level and $h = 1.036\times10^{-4}$ m^{-1} is a constant.

The Earth's surface curvature, as well as its rotation, can be accounted for in ballistic trajectories by corrections to the ground-based Cartesian coordinates and the **g** vector components. All these effects, as well as the Coriolis acceleration, are significant only for very long trajectories and are neglected in the remainder of this study. Notice that in Eq. 46, we used $\mathbf{g} = -g\mathbf{z}$ (with g = 9.8 m/s^2).

The aerodynamic coefficients mentioned in a previous paragraph have a complex dependence on the Mach number (the ratio of the projectile velocity to the speed of sound), which cannot be described by a simple closed-form expression. Typically, this dependence is captured in lookup tables, based primarily on experimental data. Moreover, these coefficients are very sensitive to the projectile's shape, meaning that separate lookup tables must be created for each type of projectile. The

aerodynamic coefficients typically vary relatively slowly with the Mach number, except for the transonic region (Mach number close to 1), where the variation may be more abrupt. In the numeric simulations performed in this report, we keep most of the aerodynamic coefficients independent of the projectile velocity. However, the coefficient associated with the most significant aerodynamic force, namely, the drag force, shows the proper variation with the Mach number, according to tables available in the literature.

Some of the aerodynamic coefficients also exhibit a variation with the angle of attack, which in the MPMT model coincides with $|\boldsymbol{\alpha}_R|$. Thus, for small angles of attack (which are usually encountered in practice),

$$C_D = C_{D0} + C_{D2} \sin^2 |\boldsymbol{\alpha}_R| \ , \tag{48a}$$

$$C_{L\alpha} = C_{L\alpha 0} + C_{L\alpha 2} \sin^2 |\boldsymbol{\alpha}_R| \ , \tag{48b}$$

$$C_{M\alpha} = C_{M\alpha 0} + C_{M\alpha 2} \sin^2 |\boldsymbol{\alpha}_R| \ , \tag{48c}$$

$$C_{Mq} = C_{Mq0} + C_{Mq2} \sin^2 |\boldsymbol{\alpha}_R| \ . \tag{48d}$$

Another aspect of integrating the differential system in Eq. 46 is specifying the initial conditions. For the velocity vector component, the initial conditions depend on the projectile direction as it leaves the muzzle of the gun. Thus, if the initial elevation and azimuth angles are ϕ_{B0} and θ_{B0} (see Fig. 6), and the initial projectile speed is V_0, then

$$V_{x0} = V_0 \cos\phi_{B0} \cos\theta_{B0} \ , \tag{49a}$$

$$V_{y0} = V_0 \sin\theta_{B0} \ , \tag{49b}$$

$$V_{z0} = V_0 \sin\phi_{B0} \cos\theta_{B0} \ . \tag{49c}$$

The initial value of the spin rate is

$$p_0 = \frac{2\pi V_0}{t_c d} \ , \tag{49d}$$

where the parameter t_c is called the rifling (twist) rate and represents the number of turns within the gun barrel in which the projectile travels a linear distance equal to its caliber (or d).

A MATLAB[16] code was developed to implement the numeric integration of Eq. 46 with initial conditions of Eq. 49. The specific algorithm employed in this code is a

4th-order Runge-Kutta procedure.[17] Once the velocity vector components are found at each time step, the ground-based Cartesian coordinates along the trajectory are calculated as

$$x(t) = x_0 + \int_0^t V_x(\tau) d\tau \ , \tag{50a}$$

$$y(t) = y_0 + \int_0^t V_y(\tau) d\tau \ , \tag{50b}$$

$$z(t) = z_0 + \int_0^t V_z(\tau) d\tau \ , \tag{50c}$$

while the spin (or roll) angle χ (as in Section 2.2) is calculated as

$$\chi(t) = \chi_0 + \int_0^t p(\tau) d\tau \ . \tag{50d}$$

In practice, all the integrals in equations in Eq. 50 are computed as running sums, each of them starting with an appropriate initial condition. Also, notice that, at each time step, the current motion parameters are used to update the air pressure via Eq. 47, the yaw of repose vector via Eq. 45, and the aerodynamic coefficients via Eq. 48.

We applied the trajectory simulation code based on the MPMT model to 2 types of projectiles: a 155-mm artillery round and a 120-mm mortar (these are the same projectiles investigated in our previous work[2,3] from a radar signature perspective). In the remainder of this section, we present the results obtained from these simulations. In all cases, the launching point is placed in the **x-y-z** coordinate system origin (meaning $x_0 = 0$, $y_0 = 0$, $z_0 = 0$).

The 155-mm artillery round is an example of spin-stabilized projectile. To find the trajectory, the full system of 4 equations in Eq. 46 was solved by the numerical algorithm. All the parameters appearing in the equations (such as mass, moments of inertia, aerodynamic coefficients, etc.) are available from public sources, primarily McCoy,[10] Carlucci and Jacobson,[13] and Balon and Komenda.[14] These parameters, together with the initial conditions, are listed in Table 1. The center of mass trajectory obtained by the MPMT model is displayed in Fig. 7. In the same figure, we illustrate the variation of the projectile velocity and orientation (elevation angle) over time during the ballistic flight.

Approved for public release; distribution unlimited.

Table 1 Physical parameters and initial conditions for the trajectory simulation examples in this section, involving a 155-mm artillery round and a 120-mm mortar

Projectile type	155-mm round	120-mm mortar
m (kg)	47.5	13.6
d (m)	0.155	0.120
I_R (kg m^2)	0.161	0.023
I_T (kg m^2)	2.106	0.232
C_D	0.249 (at Mach = 2)	0.119 (at Mach = 0.7)
$C_{L\alpha}$	2.41	2.00
$C_{Np\alpha}$	0.51	N/A
C_{lp}	–0.024	N/A
$C_{M\alpha}$	4.65	–2
C_{Mq}	–26	–22
V_0 (m/s)	564	243
p_0 (rad/s)	1143	0
ϕ_{B0} (°)	40	50
θ_{B0} (°)	0	0

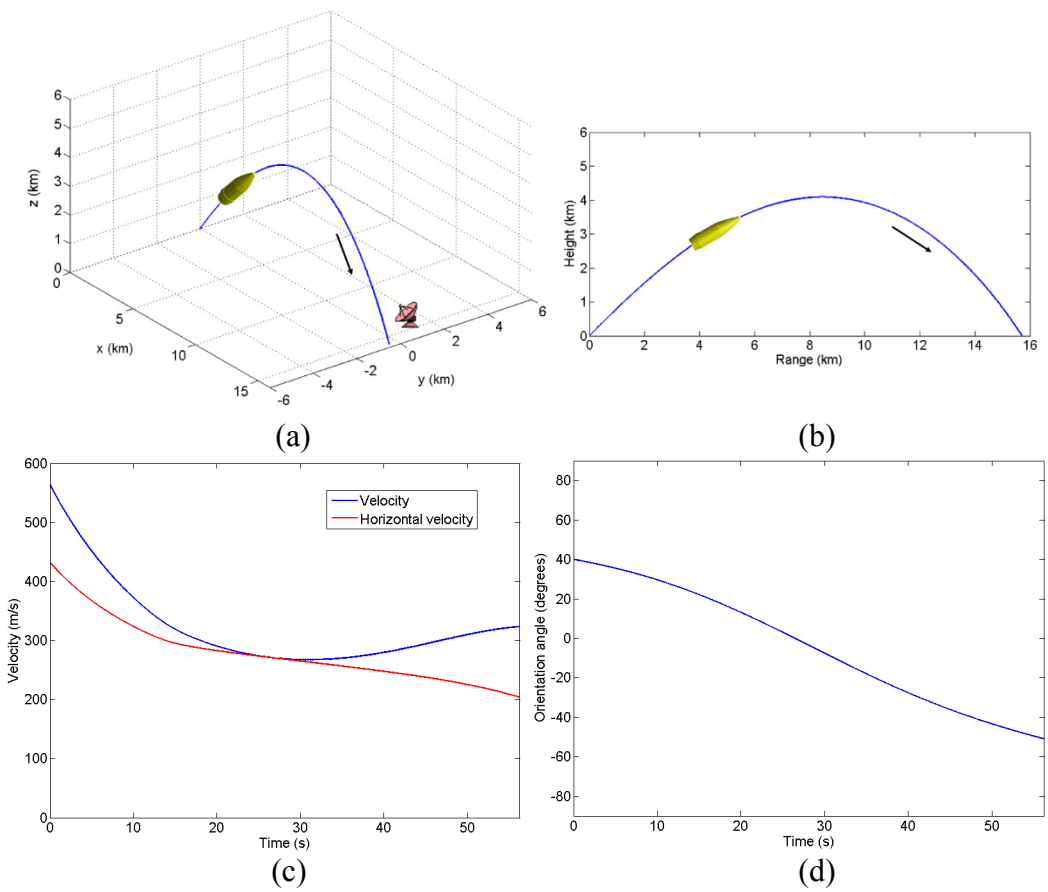

Fig. 7 Various ways of describing the simulated 155-mm artillery round ballistic trajectory and its parameter variation vs. time: a) 3-D trajectory curve, b) height vs. range curve, c) velocity components vs. time, and d) projectile orientation angle ϕ_B vs. time. Figure 7a shows the approximate radar location in the simulations in Section 4.1.

The 120-mm mortar is an example of fin-stabilized projectile. This projectile is not intended to spin during flight, and any kind of inadvertent rolling motion is rapidly damped. Since $p = 0$, Eq. 46d can be dropped from the system, leaving only the velocity vector components to solve for. The mortar parameters involved in the MPMT model equations were also obtained from publicly available sources and are listed in Table 1. Graphic representations of the trajectory, as well as the time variation of the mortar velocity and orientation, are shown in Fig. 8.

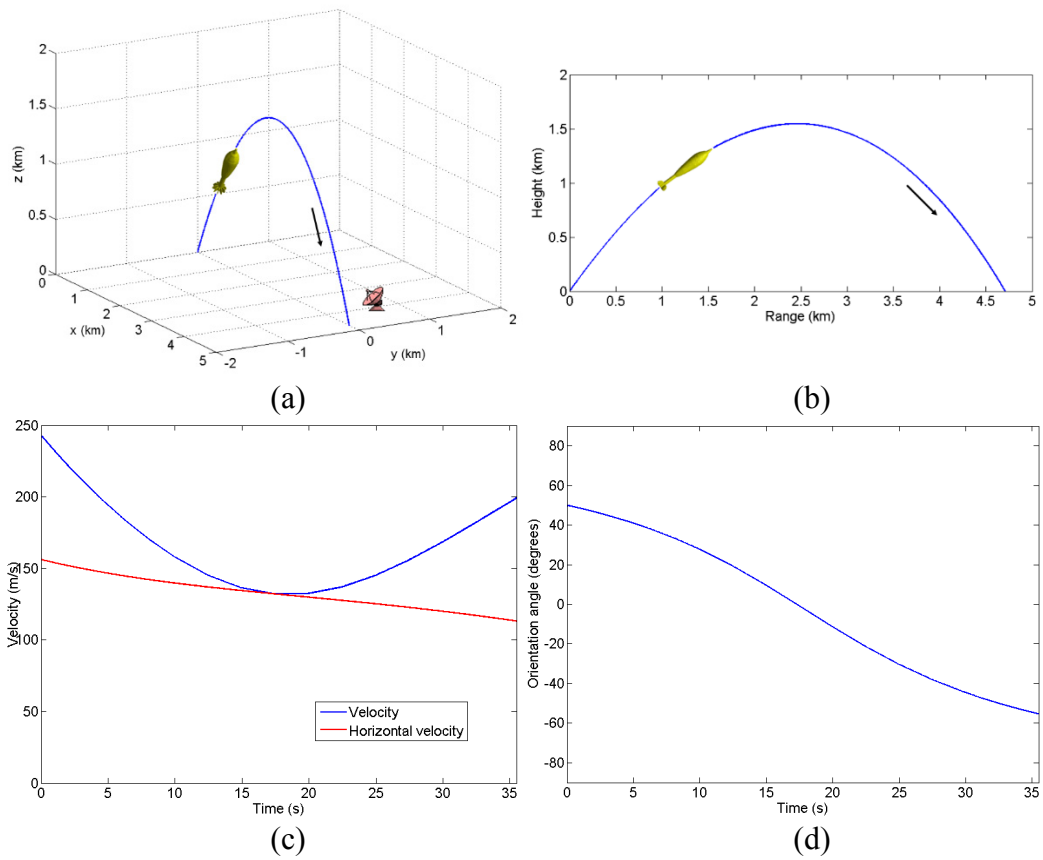

Fig. 8 Various ways of describing the simulated 120-mm mortar ballistic trajectory and its parameter variation vs. time: a) 3-D trajectory curve, b) height vs. range curve, c) velocity components vs. time, and d) projectile orientation angle ϕ_B vs. time. Figure 8a shows the approximate radar location for the simulations in Section 4.2.

3.2 Epicyclic Motion of Flying Projectiles

As discussed in the previous section, the MPMT model does not account for the transient pitching and yawing motion of the projectile during flight. Nevertheless, this well-documented phenomenon is consistently encountered in experimental ballistic data, as well as predicted by the more rigorous 6 DOF model. Although the typical amplitude of these motion components is relatively small, on the order of a few degrees, they may have a rather large impact on the time-varying radar

signature of the in-flight projectile. Therefore, to properly characterize this radar signature, our trajectory model must account for the transient pitching and yawing motion. The procedure adopted here superposes these 2 motion components as obtained from the LA model[10] to the MPMT model solution.

The analysis in this section is valid for spin-stabilized projectiles only; a similar treatment can be established for the pitching and yawing motions of fin-stabilized projectiles, but these are not considered throughout this report. As shown in McCoy[10] using the 6 DOF model, in most cases of practical interest, the pitching/yawing motion of a mortar is rapidly damped during the ballistic flight (over a duration of 2–3 s), making this analysis less important for radar signature calculation purposes.

The pitch and yaw angles (α and β, respectively) were introduced in Section 2.2 (see Fig. 4a). In the assumption that α and β are small, the unit vector of the projectile's symmetry axis, $\mathbf{k}_1$, can be written approximately as

$$\mathbf{k}_1 \cong \alpha\mathbf{i} + \beta\mathbf{j} + \mathbf{k} \,. \tag{51}$$

This equation shows that α and β are the coordinates of the $\mathbf{k}_1$ unit vector in the **i-j** plane. In other words, as the time progresses, the trace described by the projectile tip in the **i-j** plane is similar (in a geometrical sense) to the trace obtained in the α–β plane (taking β as the abscissa and α as the ordinate).

Next, we introduce the complex variable $\xi = \alpha + j\beta$ (also called complex yaw). The differential equation characterizing ξ according to the LA model is[10]

$$\ddot{\xi} + (H - jP)\dot{\xi} - (M + jPT)\xi = -jPG \;, \tag{52}$$

where

$$H = \frac{\rho S V}{2m}\left(C_{L\alpha} - \frac{md^2\left(C_{Mq} + C_{M\dot{\alpha}}\right)}{I_T}\right) , \tag{53a}$$

$$P = \frac{I_R p d}{I_T V} \;, \tag{53b}$$

$$M = \frac{\rho S V^2 d}{2I_T} C_{M\alpha} \;, \tag{53c}$$

$$T = \frac{\rho S V}{2m}\left(C_{L\alpha} + \frac{md^2}{I_R} C_{Mp\alpha} \right) , \tag{53d}$$

$$G = \frac{gd \cos\phi_B}{V^2} . \tag{53e}$$

In these equations, we introduced the following new symbols: I_T for the transversal moment of inertia and $C_{M\dot{\alpha}}$ for the pitch moment derivative coefficient. Deriving Eq. 51 involves neglecting several higher-order terms—these approximations are valid in the assumption of a small angle of attack.[10] Additionally, to obtain a linear equation in ξ, only the constant terms are retained in the expressions of the aerodynamic coefficients (Eq. 48), while the angle-dependent terms are neglected. In Eq. 51, all coefficients (H, M, P, T and G) vary slowly in time, via the parameters V, p, and ϕ_B.

The general solution to Eq. 52 can be written as

$$\xi(t) = A_1 \exp\left(j\left(\psi_1(t) + \psi_{10}\right)\right) + A_2 \exp\left(j\left(\psi_2(t) + \psi_{20}\right)\right) + j\beta_R(t) , \tag{54}$$

with the real constants A_1, A_2, ψ_{10} and ψ_{20} determined by the initial conditions. The solution in Eq. 54 includes 2 oscillatory (or transient) terms and a slowly varying (or steady-state) term. Furthermore,

$$\dot{\psi}_1(t) = \omega_1 + j\lambda_1 = \frac{1}{2}\left[P + jH + \sqrt{P^2 - 4M - H^2 - 2jP(2T - H)}\right] , \tag{55a}$$

$$\dot{\psi}_2(t) = \omega_2 + j\lambda_2 = \frac{1}{2}\left[P + jH - \sqrt{P^2 - 4M - H^2 - 2jP(2T - H)}\right] , \tag{55b}$$

$$\beta_R(t) = \frac{PG}{M + jPT} . \tag{56}$$

The validity of the solution given by Eqs. 54–56 hinges on the fact that $\omega_{1,2}$, $\lambda_{1,2}$, and β_R are all slow-varying functions of time.

After further manipulations of the expressions in Eq. 56 and neglecting some higher-order terms, we obtain

$$\omega_1 = \frac{1}{2}\left[P + \sqrt{P^2 - 4M}\right] , \tag{57a}$$

$$\omega_2 = \frac{1}{2}\left[P - \sqrt{P^2 - 4M}\right] , \tag{57b}$$

Approved for public release; distribution unlimited.

$$\lambda_1 = \frac{1}{2}\left[H - \frac{P(2T - H)}{\sqrt{P^2 - 4M}} \right], \tag{57c}$$

$$\lambda_2 = \frac{1}{2}\left[H + \frac{P(2T - H)}{\sqrt{P^2 - 4M}} \right]. \tag{57d}$$

For typical scenarios, we have $P^2 >> M$ and $M >> PT$; therefore, the following simple expressions are good approximations to Eqs. 58 and 57:

$$\omega_1 \cong P = \frac{I_R}{I_T} p \ , \tag{58a}$$

$$\omega_2 \cong \frac{M}{P} = \frac{\rho S d V^2 C_{M\alpha}}{2 I_R p} \ , \tag{58b}$$

$$\lambda_1 \cong H - T = -\frac{\rho S V d^2}{2}\left(\frac{C_{Mq} + C_{M\dot{\alpha}}}{I_T} + \frac{C_{Mp\alpha}}{I_R} \right), \tag{58c}$$

$$\lambda_2 \cong T = \frac{\rho S V}{2m}\left(C_{L\alpha} + \frac{m d^2}{I_R} C_{Mp\alpha} \right), \tag{58d}$$

$$\beta_R(t) \cong \frac{PG}{M} = \frac{2 I_R p g \cos\phi_B}{\rho S d V^3 C_{M\alpha}} \ . \tag{59}$$

By separating the real and imaginary parts, we can recast the solution in Eq. 54 as

$$\begin{aligned} \alpha(t) = {} & A_1 \exp\left(-\int_0^t \lambda_1(\tau) d\tau \right) \cos\left(\int_0^t \omega_1(\tau) d\tau + \psi_{10} \right) \\ & + A_2 \exp\left(-\int_0^t \lambda_2(\tau) d\tau \right) \cos\left(\int_0^t \omega_2(\tau) d\tau + \psi_{20} \right) \end{aligned}, \tag{60a}$$

$$\begin{aligned} \beta(t) = {} & A_1 \exp\left(-\int_0^t \lambda_1(\tau) d\tau \right) \sin\left(\int_0^t \omega_1(\tau) d\tau + \psi_{10} \right) \\ & + A_2 \exp\left(-\int_0^t \lambda_2(\tau) d\tau \right) \sin\left(\int_0^t \omega_2(\tau) d\tau + \psi_{20} \right) + \beta_R(t) \end{aligned}. \tag{60b}$$

The physical interpretation of the angular motion described in Eq. 60 is the following: both the pitch and yaw angle variations in time are characterized by 2

transient terms consisting of damped oscillations of variable instantaneous frequencies, while the yaw angle has a steady-state component with slow time variation, β_R, which is the same as the yaw of repose encountered in Section 3.1. Notice that the expressions of $|\boldsymbol{\alpha}_R|$ in Eq. 45a and β_R in Eq. 59 are identical; they imply that, for a spin-stabilized projectile, the yaw of repose vector is perpendicular to the velocity vector and has a horizontal (yaw) component only. Since $\omega_1 > \omega_2$, the first oscillatory term is called the "fast mode", whereas the second oscillatory term is called the "slow mode". To avoid dynamic instabilities, we must have $\lambda_1, \lambda_2 > 0$.[10]

As a numerical example, for a 155-mm artillery round with V = 550 m/s and p = 1100 rad/s at ground level (ρ = 1.225 kg/m^3), we obtain ω_1 = 84.1 rad/s, ω_2 = 14.2 rad/s, λ_1 = 1 s^{-1}, and λ_2 = 0.388 s^{-1}. This means that both oscillation modes are damped with time constants on the order of a few seconds. However, one should keep in mind that the LA model makes a number of approximations by neglecting nonlinear aerodynamic effects; consequently, the estimates of the damping factors based on this model are not very reliable to use in numerical simulations of the projectile motion. The nonlinear effects turn out to have a large influence on the time variation of the oscillation amplitudes[10]; nevertheless, accounting for these effects is beyond the scope of this study. The 6 DOF models, as well as experimental data, indicate that, for spin-stabilized artillery shells, the fast mode dampens with a typical time constant of 5 to 10 s, whereas the slow mode's amplitude decreases as the projectile approaches the apogee and increases again on the way to the ground impact.[10] In the numerical examples in Section 4, we choose damping time constants larger (or λ_1 and λ_2 smaller) than the results of calculations by Eqs. 58c and 58d to better emphasize the effect of these oscillations on the dynamic target RCS.

The initial conditions (the constants A_1, A_2, ψ_{10}, and ψ_{20}) are random to a large extent and depend on specific asymmetries in the construction of the gun barrel and projectile. Here, we follow the guidelines in McCoy[10] and choose these parameters consistent with typical initial pitch and yaw angles observed in live-fire experiments.

Figure 9 illustrates the trajectory described by the projectile tip in a plane perpendicular to the velocity vector (the **i-j** plane in Fig. 6), as we look along the positive **V** vector direction, over the first 1-s time interval. In this example, we chose ω_1 = 84.1 rad/s, ω_2 = 14.2 rad/s, λ_1 = 0.1 s^{-1}, λ_2 = 0.01 s^{-1}, A_1 = 1°, A_2 = 2°, ψ_{10} = 45°, and ψ_{20} = 120°. Figure 9a shows the curve described in the 3-D space (**i-j-k** coordinate system), while Fig. 9b shows its projection onto the **i-j** plane. As previously explained, the projectile tip coordinates in this plane are proportional to

β and α, respectively. Notice that, since the ratio between ω_1 and ω_2 is not an integer (although it is close to 6), the overall motion is not completely periodic, meaning that each new cycle is slightly shifted (in angle) as compared to the previous one. Also, because of the damping, the motion radius decreases with time (although this is hardly noticeable over the short time interval considered here). There is a small offset along the abscissa (**j** axis) due to the presence of the yaw of repose β_R. Numeric evaluations show that this angle is very small, typically a fraction of 1°. Consequently, it is not accounted for when we compute the orientation of the projectile; however, this angle still needs to be updated via Eq. 45a at each time step while solving the system in Eq. 46.

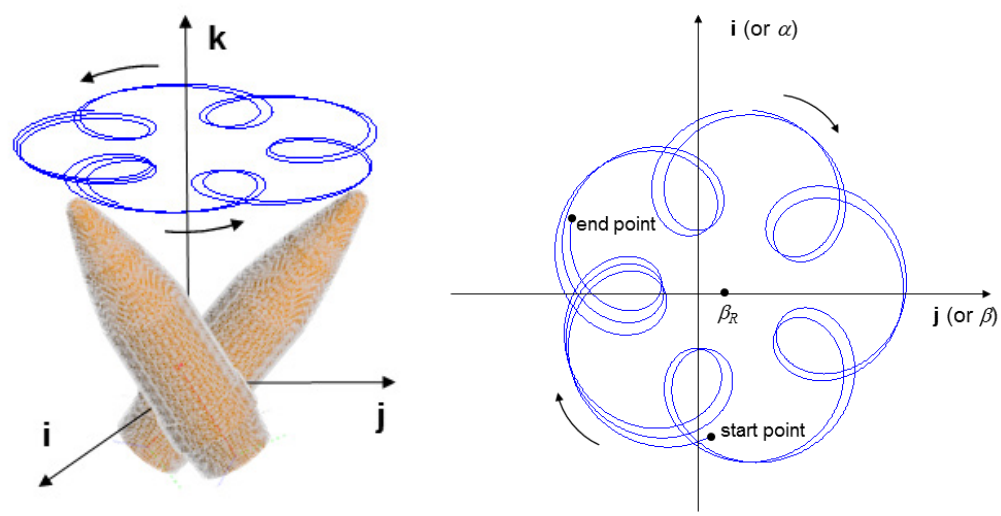

(a) (b)

Fig. 9 Trajectory described by the 155-mm projectile tip in the i-j plane over a 1-s interval. a) 3-D view and b) view in the i-j plane. The pitch and yaw angles in Fig. 9a are exaggerated (not to scale). In Fig. 9b, the observer looks along the k axis, in the positive direction.

There is a strong analogy between the motion of a spinning ballistic projectile in the mobile **i-j-k** frame and that of a spinning top in the fixed **x-y-z** ground frame. The pitch and yaw motions of the projectile can also be interpreted in terms of Euler's angles[9]—in that case, we describe the motion as made of precession and nutation components instead of pitch and yaw. Although the epicyclic motion of the flying ballistic projectile, as well as the SPY transformations in Section 2.2 can be reformulated using the precession and nutation concepts, we preferred the pitch-yaw formulation, which is typical for the treatment found in ballistics-related texts.

Approved for public release; distribution unlimited.

4. Numeric Examples

4.1 Dynamic RCS of an In-Flight 155-mm Artillery Round

The first numerical example of the dynamic RCS calculation involves a 155-mm artillery round. This is a spin-stabilized projectile; therefore, its ballistic motion model includes both the center of mass trajectory (computed by the MPMT model) and the SPY motion components (derived by the LA model). Notice that this projectile is rotationally symmetric (with respect to the **k** axis in Fig. 2b), so its radar signature is independent of the azimuth aspect angle ϕ.

In this section, we use the center of mass trajectories presented in Section 3.1. For the epicyclic motion of the 155-mm round, we use the same parameters as in the numeric example in Section 3.2 employed in generating the curves in Fig. 9. As mentioned in the previous section, the LA epicyclic motion model is not entirely realistic—in particular, its amplitude variation over time is too simplistic, since it fails to take into account some important nonlinear effects. Nevertheless, the purpose of our simulations is to evidence some interesting qualitative phenomena regarding the time variation of the dynamic radar signature. From this perspective, the trajectory model presented here is adequate.

The radar is placed at coordinates x_R = 15 km, y_R = 1 km, and z_R = 2 m. The maximum range of the trajectory is 15.7 km, while the drift is –362 m, so the projectile lands past the radar location (in the x direction) and to the side (in the y direction). The flight time is approximately 56.3 s. This simulation is typical for a scenario where the radar is placed in the proximity of the perimeter presumably under artillery attack. As one can expect, the dynamic radar signature may change significantly if the radar-to-trajectory range and orientation is modified. However, the signature computation method remains the same in all these scenarios.

Since some of the most important calculations outlined in Sections 2.2, 2.3, and 2.4 involve finding relative angles between the radar, projectile, and ground, we think it is informative to present the variation of some of these angles during the ballistic flight. Thus, in Fig. 10a, we plot on the same graph the projectile-to-ground elevation angle ϕ_B (the same as in Fig. 7d), the radar-to-projectile elevation angle θ (given by Eq. 10), and the radar-to-ground grazing angle γ (given by Eq. 37). The oscillating nature of the ϕ_B and θ angles reflects the epicyclic motion of the projectile axis during flight. However, since the radar beam tracks the projectile center of mass (whose trajectory is smooth), the grazing angle does not exhibit oscillations. In Fig. 10b, we show the polarization rotation angle η, which is defined by Eq. 21; this angle also exhibits fast oscillations during the projectile flight.

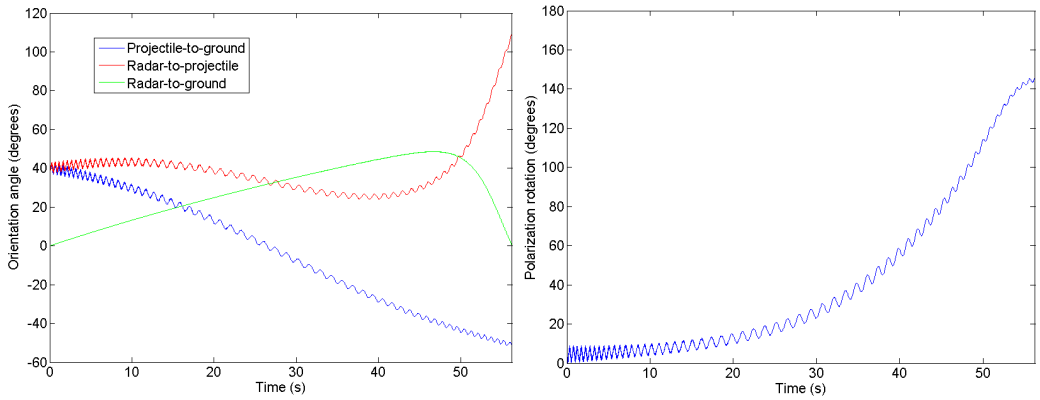

(a) (b)

Fig. 10 Relative angles between the radar, projectile orientation, and ground obtained in the trajectory simulations of the 155-mm artillery round, showing: a) the ϕ_B, θ and γ angles, and b) the polarization rotation angle η

Next, we present the variation of the RCS with time during the ballistic flight. The graphs shown here cover 4 radar bands (L, S, C, and X), with the following frequencies: 1.3 GHz for the L-band, 2.4 GHz for the S-band, 5.6 GHz for the C-band, and 9.5 GHz for the X-band, as well as the V-V and H-H polarization combinations. We plot separately the RCS obtained by ignoring the SPY motion components of the projectile (Fig. 11) and the RCS that includes the SPY components (Fig. 12). Note that the radar wave polarizations (V-V or H-H) are defined relative to the ground-based radar frame (*G*).

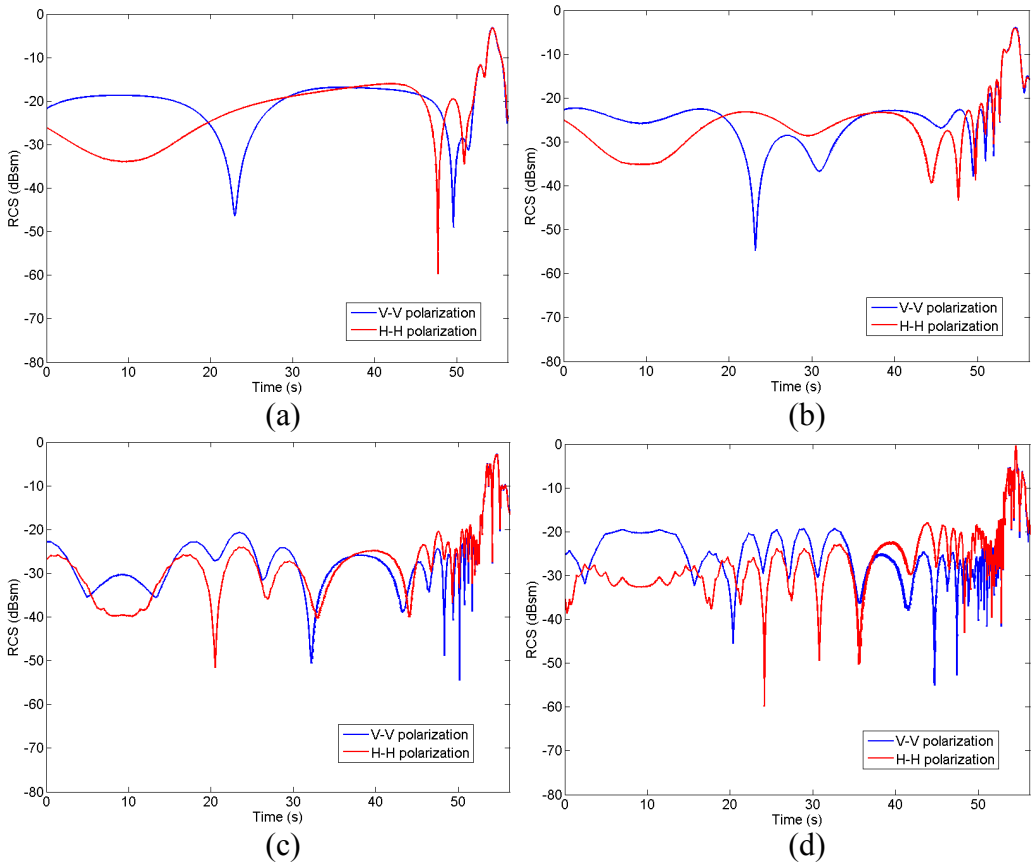

Fig. 11 Dynamic RCS vs. time curves obtained for the simulated trajectory of the 155-mm artillery round that does not account for the SPY motion components: a) L-band, b) S-band, c) C-band, and d) X-band

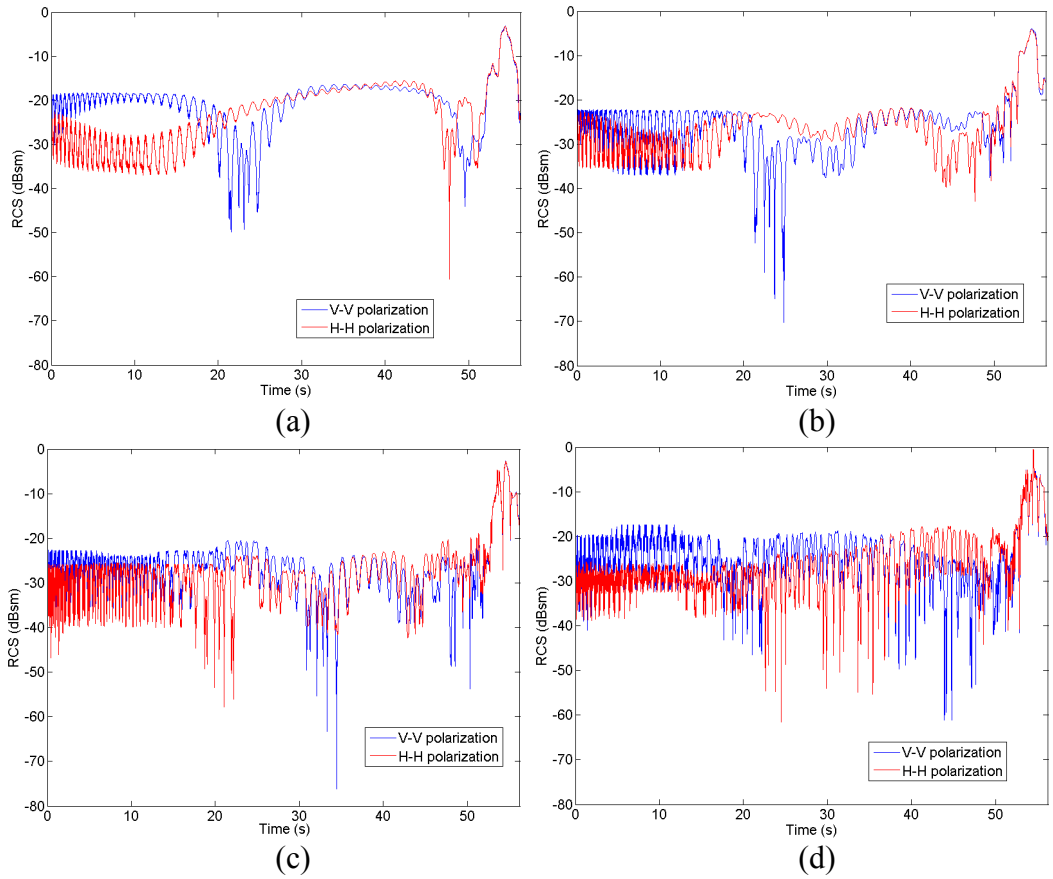

Fig. 12 Dynamic RCS vs. time curves obtained for the simulated trajectory of the 155-mm artillery round that includes the SPY motion components: a) L-band, b) S-band, c) C-band, and d) X-band

The dynamic RCS plots indicate that, on the average, the projectile's signature stays fairly flat during the ballistic flight, except for the last few seconds of the trajectory. The reason for this is that, most of the time, the radar "sees" the projectile close to the nose-on aspect, so the RCS changes very little; only at close range and steep projectile descent angle (during the last few seconds of the flight) does the aspect change to near-broadside. Moreover, the oscillations of the RCS curves in Fig. 11 are fairly slow for most of the trajectory, but become more rapid at its end—this effect can be explained by the fact that the RCS changes more rapidly with the aspect angle near broadside than at nose-on orientation. As expected, the RCS exhibits faster oscillations as the frequency increases (compare, for instance, the X- and L-band curves in Fig. 11).

The graphs in Fig. 12 clearly show the impact of the epicyclic motion of the 155-mm round on the dynamic RCS. We notice 2 oscillations induced by this motion: a fast mode with a frequency of about 13 Hz that lasts for about 10 s and a slow mode with a frequency of about 2 Hz that lasts during the entire flight. Notice

that the frequency of these oscillations in the RCS curves is independent of the radar frequency band. It can be shown that the oscillation frequencies are also independent of the relative orientation of the radar with respect to the trajectory. Possible ways to exploit this signature feature for target discrimination or identification will be investigated in a separate study.

In terms of RCS magnitude, the results in Figs. 11 and 12 are consistent with our previous findings,[2] which suggest that, on the average, all 4 radar bands offer approximately the same signature strength. When we compare the V-V and H-H polarizations, we notice that the V-V case consistently exhibits a higher RCS early during flight (approximately the first 20 s), after which the 2 signatures become comparable. An explanation is the fact that, early during the ascending part of the ballistic trajectory, the projectile axis is closely aligned with the electric-field vector for the V-V case. Since the projectile axis is also parallel to most of the target's physical boundary, this alignment creates a stronger backscattering response than in the H-H case. When the projectile aspect approaches broadside, the V-V and H-H signatures tend to become identical.

We further analyzed the radar return from the in-flight projectile by calculating the received radar power according to Eqs. 32 or 33. We considered a radar transmitted (peak) power of P_t = 8 kW (or 70 dBm). For the computation of the propagation factor F[4], we used a ground dielectric constant $\varepsilon_r = 8$. The radar antenna model that we choose is key in comparing the radar performance for different frequency bands. Thus, if we choose a fixed antenna gain for all bands, $G_t = G_r$ = 40 dB, the graphs in Fig. 13, based on Eq. 32, suggest that the performance is better at lower frequencies (largest received power for L-band). However, if our model assumes the same antenna aperture for all bands, $A_t = A_r = 4$ m^2, the graphs in Fig. 14, based on Eq. 33, lead us to the opposite conclusion: the performance is better at higher frequencies. These differences are clearly dictated by the presence of the factor λ^2 in the numerator in Eq. 32 and in the denominator in Eq. 33. As a side note, one should consider the fact that, in the X-band, a gain of 40 dB can be achieved with a 0.8-m^2 antenna aperture, whereas, in the L-band, obtaining the same gain requires a 42-m^2 aperture. For completeness, in Eq. 34 we used an antenna gain that varies with the squint angle θ_A as

$$G(\theta_A) = \frac{G(0)}{2}\left(1 + \cos\left(\pi \frac{\theta_A}{\theta_{HB}}\right)\right) . \tag{61}$$

In this equation, the main antenna beam was represented as a Hanning window with respect to the angle θ_A, where θ_{HB} = 5° is the half-beamwidth (to the first zero-intercept point). While this is just a generic model of the antenna pattern (does not

represent any specific antenna design), it is representative enough for the purpose of our analysis.

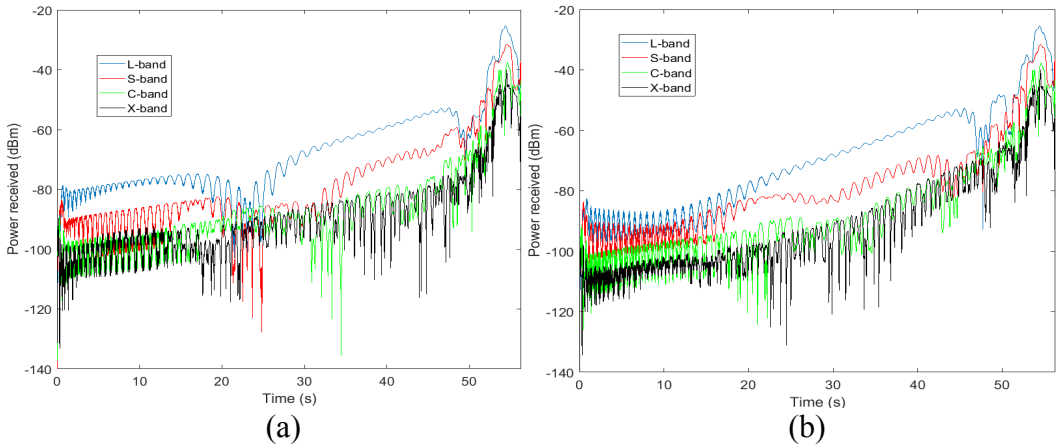

Fig. 13 Received radar power vs. time for the in-flight 155-mm artillery round, assuming the fixed gain model in all 4 frequency bands, showing a) V-V polarization and b) H-H polarization

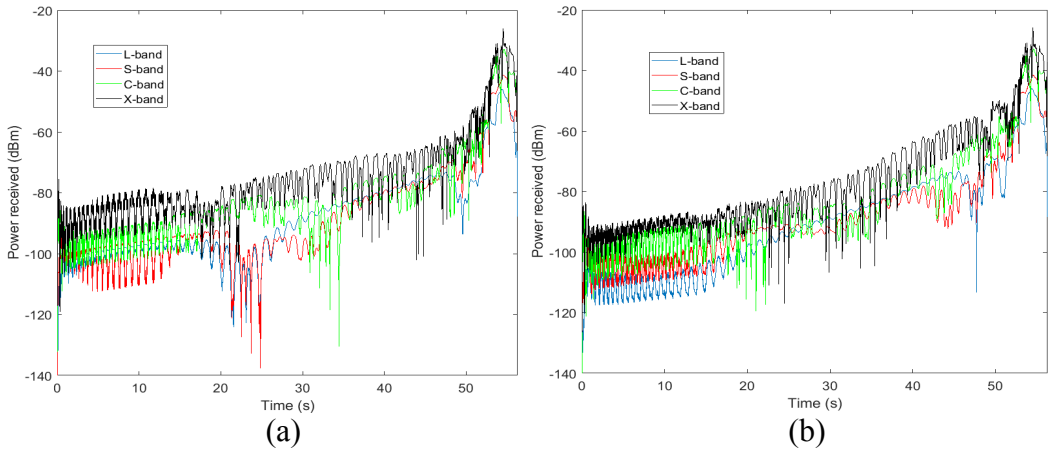

Fig. 14 Received radar power vs. time for the in-flight 155-mm artillery round, assuming the fixed aperture model in all 4 frequency bands, showing a) V-V polarization and b) H-H polarization

The increasing trend of the received power with time in Figs. 13 and 14 can be largely explained by the reduction in radar-to-projectile range as the projectile gets closer to the final impact. More interestingly, we notice a fairly large oscillation of the power for the first 1 or 2 s of the flight. This is the effect of the propagation factor F^4, which manifests itself only at very low grazing angles. We can demonstrate that by separately plotting F^4 versus time, for all frequency bands and both polarizations, in Fig. 15. This factor is almost identical for V-V and H-H polarizations due to the fact that the ground reflection coefficient is approximately the same (close to –1) for both wave polarizations at small grazing angles.[7] Notice

the large oscillations of F^4 for the first 1.5 s, involving swings of 20 to 30 dB, which can have a dramatic effect on the radar detection performance during that time interval. Subsequently, the propagation factor stabilizes to a value of 1, since the ground-bounced rays start to propagate outside the antenna main beam, so they are mostly suppressed. The oscillations in the propagation factor reappear at the very end of the flight, but at that point they are swamped by larger oscillations in the target signature that were previously explained. A closer look at the power variations for the first few seconds of the flight is presented in Fig. 16, where we used the constant gain model in the radar equation. Interestingly, these curves clearly capture the 3 types of RCS oscillations discussed in this section: the fast and slow modes due to the epicyclic motion, as well as the variations in F^4 at very close to grazing angles.

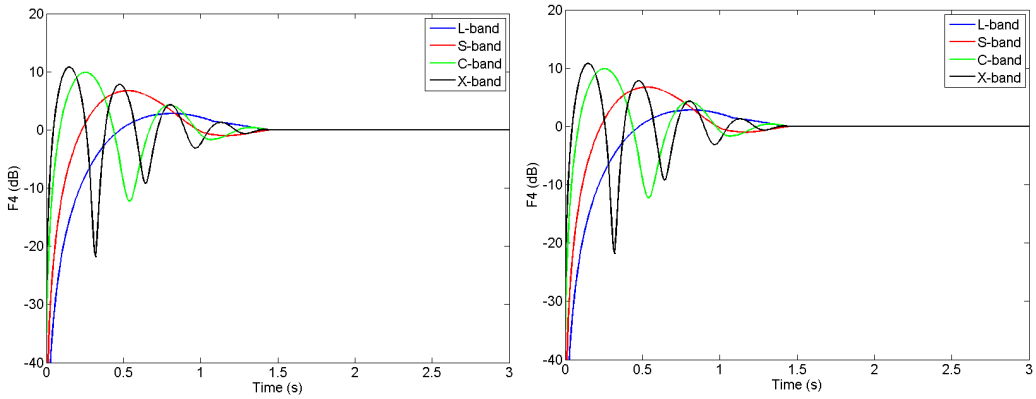

(a) (b)

Fig. 15 Propagation factor F^4 during the first 3 s of the 155-mm round ballistic flight, for all 4 frequency bands and a) V-V polarization and b) H-H polarization

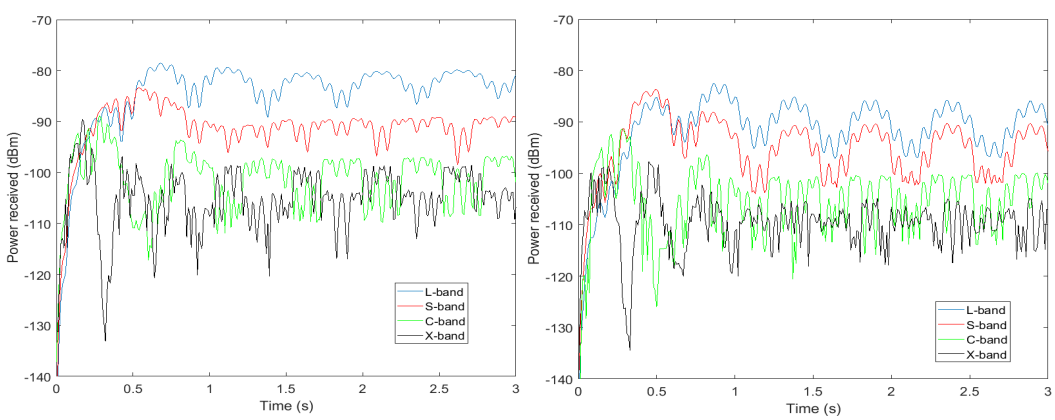

(a) (b)

Fig. 16 Received radar power during the first 3 s of the 155-mm artillery round ballistic flight, assuming the fixed gain model in all 4 frequency bands, showing a) V-V polarization and b) H-H polarization

One should keep in mind that the target signature analysis presented in this report is only one aspect of the radar system performance analysis. A complete assessment of the latter should include gains/losses induced by various system components and signal processing schemes, as well as the accuracy of the radar measurements. Other considerations (size, cost, impact of manufacturing errors, maintainability, etc.) must also be taken into account when making design decisions.[7]

4.2 Dynamic RCS of an In-Flight 120-mm Mortar

The other numeric example of the dynamic RCS considers the 120-mm mortar. Since this is a fin-stabilized ballistic projectile, we are not concerned with the SPY motions, but only with the motion of the center of mass, as simulated by the MPMT model. As with the 155-mm artillery round, we used the same trajectory as that simulated in Section 3.1. In this case, the radar is placed at coordinates x_R = 4.5 km, y_R = 0.5 km, and z_R = 2 m. The flight time is 35.5 s, the maximum range is 4.7 km, and there is no trajectory drift in this case.

Although the dynamic RCS analysis of the mortar is simplified as compared to the artillery round by the absence of the epicyclic motion, the additional feature that we need to take into account is the asymmetry introduced by the mortar's fins. In this case, the radar signature is sensitive to the relative azimuth angle ϕ. In turn, this angle depends on the initial roll angle χ_0, which appears in Eq. 50d (notice that, since $p = 0$, the roll angle χ stays constant during the flight). One aspect we want to investigate is the impact of the initial roll angle (which is typically unknown in advance) on the dynamic RCS curves.

Figure 17a shows the variation of the same angles as in Fig. 10a (namely, ϕ_B, θ and γ) for the mortar trajectory. These curves are very similar to the ones in Fig. 10a, except that they do not exhibit the fast oscillations induced by epicyclic motion. Notice that these 3 angles do not depend on χ_0. Figure 17b shows the variation of the azimuth aspect angle ϕ, for 2 different values of χ_0: 0° and 90°. (Note: Since the mortar model considered in this study has 10 fins, the target aspects "seen" by the radar for the 2 orientations are different). As expected, there is a direct dependency between the 2 angles—note that the difference between the 2 curves describing ϕ stays very close to 90° during the entire trajectory.

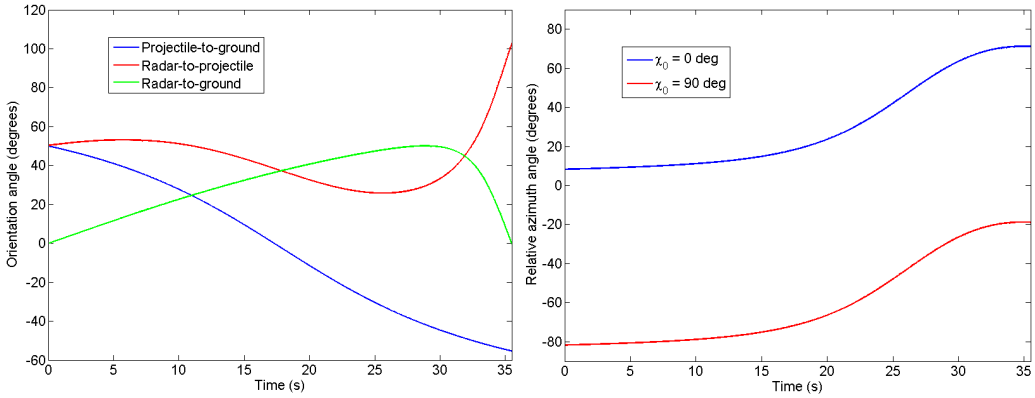

(a) (b)

Fig. 17 Relative angles between the radar, projectile orientation, and ground obtained in the trajectory simulations of the 155-mm artillery round, showing a) the ϕ_B, θ, and γ angles and b) the ϕ angle for 2 values of χ_0

Next, we look at the RCS variation over time, in the 4 frequency bands, and different values of χ_0, in Fig. 18 (V-V polarization only). The 3 cases in each graph represent $\chi_0 = 0°$ (blue line), $\chi_0 = 90°$ (red line), and the average RCS (green line) taken over all possible χ_0 values (the average is computed in terms of scattering matrix elements). For the L- and S-bands, the 3 curves are identical. For the C- and X-bands, some differences start to appear between the 3 cases, but they are generally small (less than 2 dB in the regions of sizeable RCS). These results, consistent with our previous findings,[3] demonstrate that the asymmetry in the mortar geometry has very little impact on its radar signature. In other words, there is very little dependence of the RCS on the azimuth aspect angle—this dependence is more pronounced as the frequency increases. Given this, as well as the fact that χ_0 is typically unknown, our subsequent results only consider the average RCS over all possible χ_0 values.

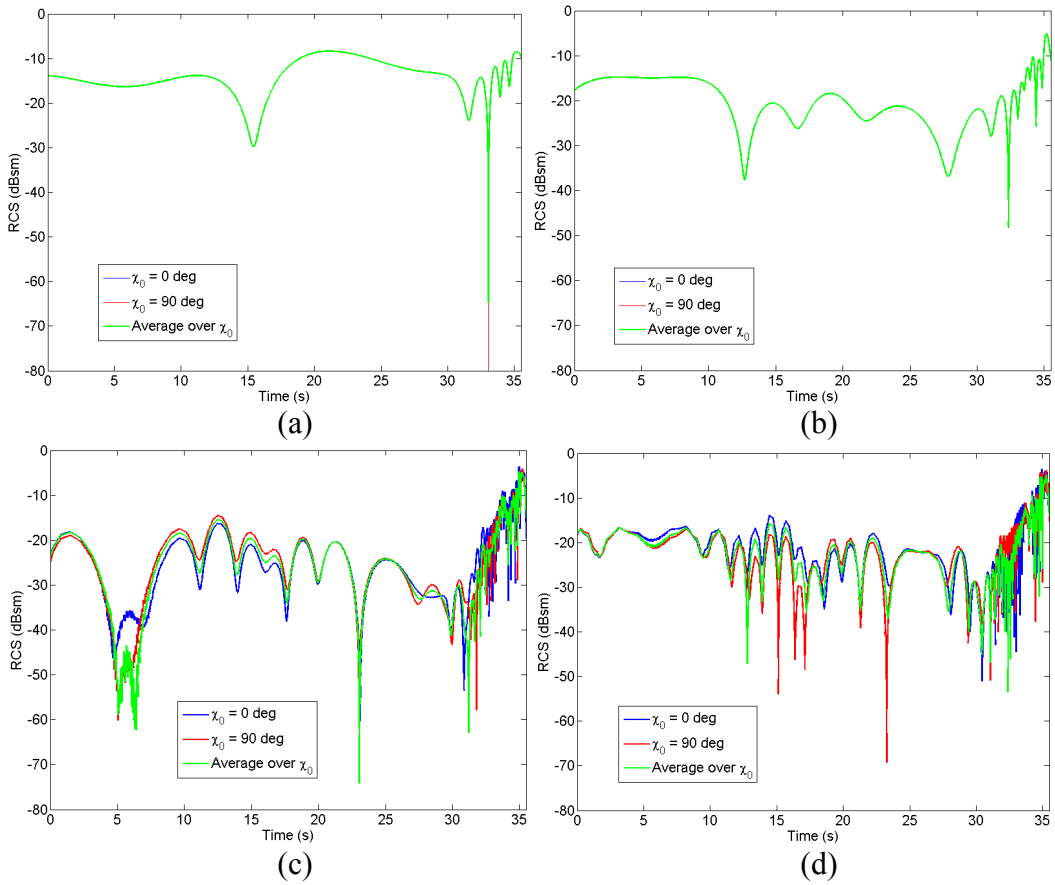

Fig. 18 Dynamic RCS vs. time curves obtained for the simulated trajectory of the 120-mm mortar, comparing various ways to account for the initial roll angle χ_0, for V-V polarization and a) L-band, b) S-band, c) C-band, and d) X-band. Note: The curves obtained for L- and S-bands are on top of one another.

The RCS versus time graphs in Fig. 19 are equivalent to those in Fig. 11, with the mention that we plotted the mean RCS over χ_0 in Fig. 19. The conclusions about the time variation of the RCS for the mortar are similar to those for the 155-mm round in the absence of the SPY motion components. However, the differences between V-V and H-H polarization, clearly visible in the early part of the 155-mm round trajectory, are less evident in the case of the mortar. One possible explanation is the more rounded shape of the mortar projectile, which makes the target response less sensitive to the radar wave polarization. In other words, the argument we made in Section 4.1 that the electric-field vector in vertical polarization is aligned with the target's boundary is no longer valid.

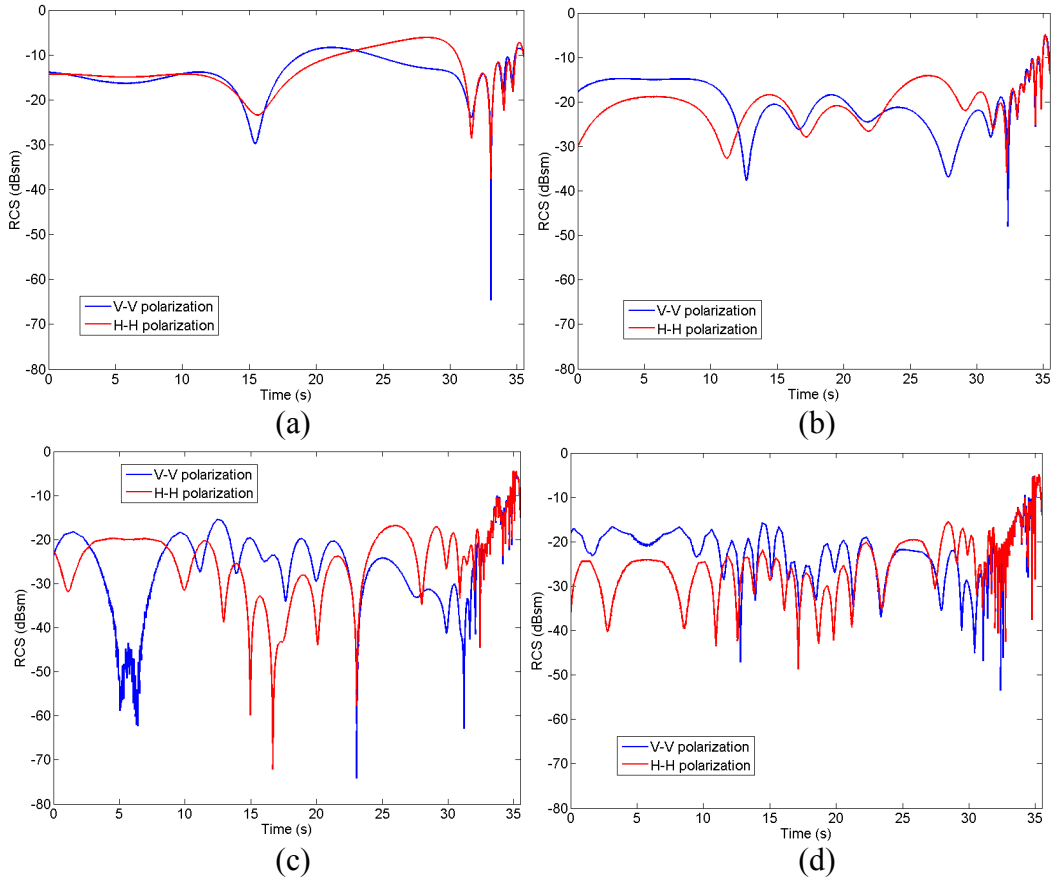

Fig. 19 Dynamic RCS vs. time curves obtained for the simulated trajectory of the 120-mm mortar, using the average over all possible angles χ_0, for a) L-band, b) S-band, c) C-band, and d) X-band

With regard to the received radar power, the results follow the same trends as for the 155-mm round. In this section, we only show the received power versus time for the fixed gain case ($G_t = G_r = 40$ dB), with the same radar parameters as in Section 4.1, in Fig. 20. Once again, we notice the large oscillations for the first 1 s of the trajectory, produced by changes in the propagation factor F^4 at close to grazing angles. The power received during this part of the trajectory is shown in closer detail in Fig. 21. Due to the steeper launch angle ϕ_{B0} (50° for the mortar vs. 40° for the 155-mm round), the time it takes for the propagation factor to stabilize to unit value is shorter in the mortar case.

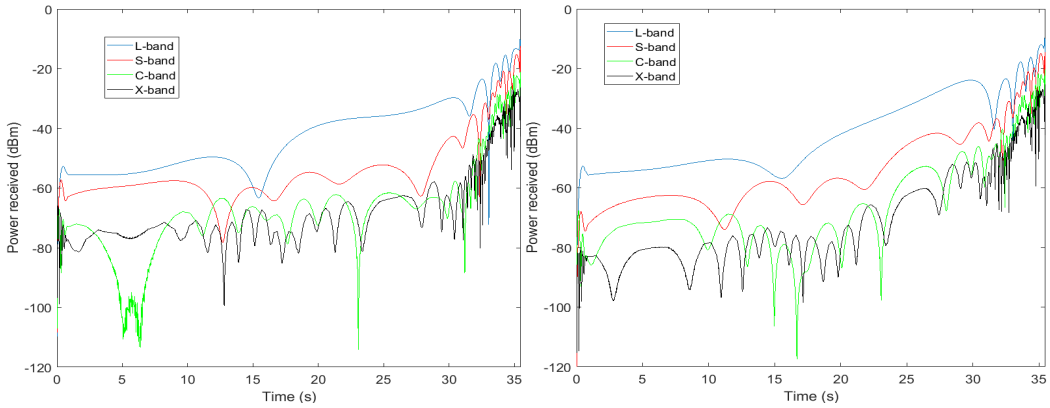

(a) (b)

Fig. 20 Received radar power vs. time for the in-flight 120-mm mortar, assuming the fixed gain model in all 4 frequency bands, showing a) V-V polarization and b) H-H polarization

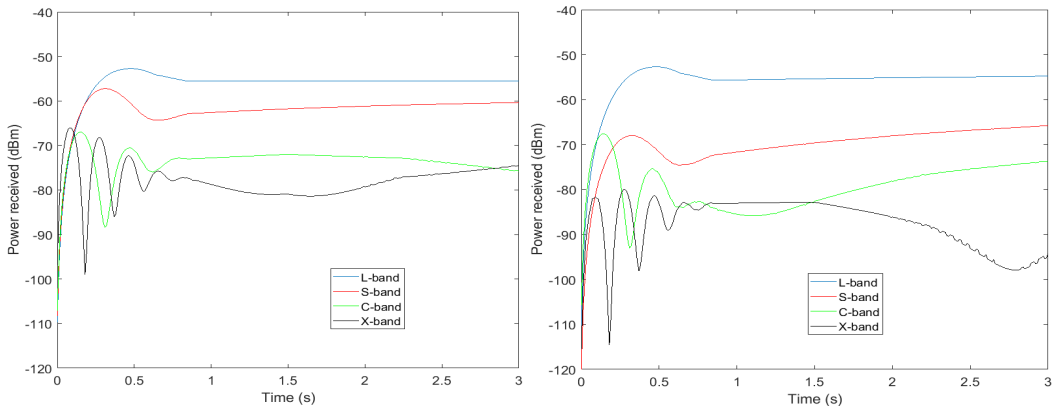

(a) (b)

Fig. 21 Received radar power during the first 3 s of the 120-mm mortar ballistic flight, assuming the fixed gain model in all 4 frequency bands, showing a) V-V polarization and b) H-H polarization

5. Conclusions

In this report, we developed a method of evaluating the radar signature of in-flight ballistic projectiles based on computer models. The method consists of 3 parts: calculating the radar signature of the projectile in a fixed position, creating a model of the ballistic trajectory, and evaluating the RCS of the in-flight projectile by performing geometrical transformations on the scattering matrix from the ground-based radar frame to the projectile frame. The first part, which employed the AFDTD radar signature software, was discussed in detail in our previous work.[2] The second and third parts were presented in Sections 2 and 3 of this report, respectively.

The ballistic trajectory simulations developed in Section 3 were based on the MPMT model. Although this model accurately predicts the center of mass trajectory, certain approximations are involved in its derivation and some motion elements (the pitching and yawing of the projectile axis) are not accounted for. Nevertheless, the pitching and yawing motions were added separately based on the LA model and turned out to have a significant impact on the radar signature of the projectile.

The method developed here allows the evaluation of the full scattering matrix of the in-flight projectiles, as well as the RCS for various polarizations. Moreover, we used the radar equation to obtain the received radar power; in this formulation, we accounted for the propagation factor F^4, which typically has a large effect at very close to grazing angles. Other issues related to the radar antenna's impact on the system performance were also discussed, although they were not included in the numerical examples in Section 4.

The numerical result section analyzes the radar signature of a 155-mm artillery round and a 120-mm mortar, for typical trajectories. The results are presented in 4 radar frequency bands (L, S, C, and X). As already shown in our previous work,[2,3] on the average, there are no significant differences in RCS among the 4 bands; nevertheless, we notice more rapid RCS variations as the frequency increases. A rigorous statistical analysis of the projectiles radar signature is deferred to a future separate study. Another important finding of the simulations in Section 4 is that the epicyclic motion of the spin-stabilized projectiles induces relatively fast variations in their RCSs during flight. The spectral analysis of these variations and its possible exploitation will be the subject of future investigations.

Finally, one should mention that the radar signature evaluation technique developed here is general, in the sense that it does not depend on the method of generating the trajectory data (whether through models with various degrees of accuracy or through measurements). The ballistic trajectory models in Section 3 were mainly developed to provide us with data that allowed us to test the radar signature calculation algorithms. Application of these algorithms to trajectories generated by more rigorous ballistic models would produce even more realistic evaluations of the projectile's radar signature, which is an important component in the overall radar system performance prediction. In the future, we hope to acquire experimental data collected by this type of radar system, for the purpose of validating the computer models.

Approved for public release; distribution unlimited.

6. References

1. Otero M, Deresh B, Teig L, Werth J, Darrah C, Hsu K, Jones D, Holder J, Cagle R. RCS modeling of projectiles for counterfire radar performance simulations. McLean (VA): MITRE Corporation (US); 2007 Jul.

2. Kenyon C, Dogaru T. Numerical computation of the radar cross section of rockets and artillery rounds. Adelphi (MD): Army Research Laboratory (US); 2015 Sep. Report No.: ARL-TR-7468.

3. Kenyon C, Dogaru T. Numerical computation of the radar cross section of a 120-mm mortar. Adelphi (MD): Army Research Laboratory (US); 2015 Nov. Report No.: ARL-TN-0716.

4. Dogaru T. AFDTD user's manual. Adelphi (MD): Army Research Laboratory (US); 2010 Mar. Report No.: ARL-TR-5145.

5. Balanis C. Advanced engineering electromagnetics. New York (NY): Wiley; 1989.

6. Ruck G, Barrick DE, Stuart WD, Krichbaum CK. Radar cross section handbook. New York (NY): Plenum Press; 1970.

7. Richards M, Scheer J, Holm W. Principles of modern radar. Raleigh (NC): SciTech Publishing; 2010.

8. Skolnik MI. Introduction to radar systems. New York (NY): McGraw Hill; 2001.

9. Foley J D, Van Dam A, Feiner SK, Hughes JF. Computer graphics: principles and practice. Boston (MA): Addison-Wesley; 1995.

10. McCoy RL. Modern exterior ballistics. Atglen (PA): Schiffer Publishing; 2012.

11. Balanis C. Antenna theory – analysis and design. New York (NY): Wiley; 1997.

12. Dogaru T, Le C. Through the wall radar simulations using polarimetric antenna patterns. Adelphi (MD): Army Research Laboratory (US); 2012 Mar. Report No.: ARL-TR-5951.

13. Carlucci DE, Jacobson S. Ballistics – theory and design of guns and ammunition. Boca Raton (FL): CRC Press; 2014.

14. Balon R, Komenda J. Analysis of the 155-mm ERFB/BB projectile trajectory. Advances in Military Technology (Czech Republic). 2001 Jan:91–114.

15. STANAG 4355, Edition 3. The modified point mass and five degrees of freedom trajectory models. Brussels (Belgium): NATO Standardization Agency; 2009 Apr.

16. MathWorks web page. Natick (MA): The MathWorks Inc.; 2016 [accessed 2016 Aug]. http://www.mathworks.com/products/matlab/.

17. Press WH, Vetterling WT, Teukolsky SA, Flannery BP. Numerical recipes in Fortran 77. Cambridge (UK): Cambridge University Press; 1992.

Approved for public release; distribution unlimited.

List of Symbols, Abbreviations, and Acronyms

3-D	3-dimensional
ARL	US Army Research Laboratory
BRL	Ballistic Research Laboratory
DOF	degrees of freedom
EM	electromagnetic
H-H	horizontal-horizontal
H-V	horizontal-vertical
LA	linear aeroballistic
LOS	line of sight
MPMT	modified point-mass trajectory
RAM	rocket, artillery, and mortar
RCS	radar cross section
SPY	spinning, pitch, and yaw
V-H	vertical-horizontal
V-V	vertical-vertical

Approved for public release; distribution unlimited.

1	DEFENSE TECH INFO CTR
(PDF)	ATTN DTIC OCA
2	US ARMY RSRCH LAB
(PDF)	ATTN IMAL HRA MAIL & RECORDS MGMT
	ATTN RDRL CIO L TECHL LIB
1	GOVT PRNTG OFC
(PDF)	ATTN A MALHOTRA
7	US ARMY RSRCH LAB
(PDF)	ATTN RDRL SER U
	A SULLIVAN
	C KENYON
	C LE
	D LIAO
	T DOGARU
	ATTN RDRL SER M
	A HEDDEN
	D WIKNER